DISCLAIMER:

This document does not meet the
current format guidelines of
the Graduate School at
The University of Texas at Austin.

It has been published for
informational use only.

The Thesis Committee for Reinaldo Jose Sabbagh
Certifies that this is the approved version of the following thesis:

Pre-injection reservoir characterization for CO_2 storage in the inner continental shelf of the Texas Gulf of Mexico

APPROVED BY
SUPERVISING COMMITTEE:

Supervisor:

Timothy Meckel

Kyle T. Spikes

Mrinal K. Sen

Pre-injection reservoir characterization for CO_2 storage in the inner continental shelf of the Texas Gulf of Mexico

by

Reinaldo Jose Sabbagh

Thesis

Presented to the Faculty of the Graduate School of

The University of Texas at Austin

in Partial Fulfillment

of the Requirements

for the Degree of

Master of Science in Geological Sciences

The University of Texas at Austin

May 2017

Dedication

To my family and friends.

Abstract

Pre-injection reservoir characterization for CO_2 storage in the inner continental shelf of the Texas Gulf of Mexico

Reinaldo Jose Sabbagh, M.S.Geo.Sci.

The University of Texas at Austin, 2017

Supervisor: Timothy Meckel

The injection of CO_2 into the subsurface (carbon capture and storage; CCS) is the most viable approach to significantly reduce industrial emissions of greenhouse gasses to the atmosphere. The inner continental shelf of the northern Gulf of Mexico has incredible potential for CO_2 storage. This study quantitatively evaluates the CO_2 storage capacity of the Lower Miocene brine-filled sandstones in the inner continental shelf of the Texas Gulf of Mexico using 3D seismic and well log data. The first part of this work investigates the relationship between elastic properties and reservoir properties (e.g., porosity, mineralogy, and pore fluid) of the Lower Miocene section using rock physics modeling and simultaneous seismic inversion. The elastic properties are related to porosity, mineralogy and pore fluid using rock physics models. These rock physics transforms are then applied to the seismically derived elastic properties to estimate the porosity and lithology away from the wells. The porosity and lithology distribution derived using this quantitative method can be interpreted to predict the best areas for CO_2 storage in the inner continental shelf of the Texas Gulf of Mexico. The second part of this work studies the effect that CO_2

has on the elastic properties of the Lower Miocene rocks using fluid substitution, amplitude variation with angle (AVA), and statistical classification to determine the ability of the seismic method to successfully monitor CO_2 injected into the subsurface. The velocities and density well logs were modeled with different fluid saturations. To characterize the seismic properties corresponding to these different fluid saturations, the AVA responses and probability density functions were calculated and used for statistical classification. The AVA modeling shows a high sensitivity to CO_2 due to the soft clastic framework of the Lower Miocene sandstones. The statistical classification successfully discriminates between brine and CO_2 saturation using Vp/Vs and P-impedance. These results shows that the Lower Miocene sandstones have the capacity to host CO_2, and that the CO_2 injected in these rocks is likely to be successfully monitored using seismic methods.

Table of Contents

List of Tables

List of Figures

Chapter 1: Introduction

1.1 INTRODUCTION

The injection of CO_2 into the subsurface (carbon capture and storage; CCS) is the most viable approach to significantly reduce industrial emissions of greenhouse gasses to the atmosphere. The CO_2 is injected mainly in saline formations or depleted oil and gas reservoirs. The intended storage reservoirs require favorable geologic properties such as high porosity and permeability, high seal capacity, and an effective trapping mechanism. The intended storage reservoir is usually below 2600 feet where the pressure and temperature of the reservoir change the phase of the CO_2 from gaseous to liquid. This is known as the supercritical phase where the CO_2 behaves as a fluid with low density, fairly low water solubility, and low viscosity (Friedman, 2007).

For CCS to be effective, the CO_2 should be monitored during and after injection to guarantee that it is safely retained underground. Among the monitoring methods for CO_2, the seismic methods provide the volumetric coverage needed to understand the distribution of CO_2 in the subsurface (McKenna et al.; 2003; Lumley, 2010; Sava, 2013). Seismic methods have been used for monitoring CO_2 sequestration in different geological scenarios through time-lapse applications. Time-lapse seismic methods attempt to quantify the difference in the seismic response before and after the injection of CO_2 (Lumley, 2010; Dvorkin et al., 2014).

Many successful CO_2 storage projects exist around the world. One of earliest industrial projects solely for CO_2 storage is the Sleipner Field in the North Sea, where the CO_2 is being injected into the Utsira Sand, a major regional saline aquifer (Chadwick et al., 2005). An extensive seismic monitoring program has been carried out over the injection

area for more than ten years. Four 3D seismic surveys were acquired for time-lapse analysis of injected CO_2 (Bickle et al., 2007). The effect of the CO_2 on the seismic data is evident. The CO_2 plume is imaged on the seismic data as a prominent multi-tier feature, comprising a number of bright sub-horizontal reflections, growing with time (Arts et al., 2008). Gassmann fluid substitution was used at Sleipner to estimate the velocities in the Utsira sand with different saturations of CO_2, obtaining a decrease in P-wave velocity (Vp) when the saturation of CO_2 increases (Chadwick et al., 2005). In many ways, the subsurface conditions of Utsira Sand are ideal for seismic monitoring: a brine-saturated, high porosity (>30%) and permeability (multi-Darcy), and relatively homogeneous clastic injection interval at relatively shallow depths. Other projects have grater challenges for imaging CO_2 injected into the subsurface.

The Otway project in Australia, for example, does not present favorable conditions for the application of time-lapse monitoring techniques. This project is the first demonstration of geological storage of CO_2 in Australia, and consisted of the injection of 66,000 tones of 80/20% CO_2-CH_4 mixture into a depleted gas reservoir (Waarre Formation) at a depth of approximately 2000 meters at the Naylor Field. The CO_2-CH_4 mixture injected into the depleted gas reservoir produces subtle changes in the 4D seismic response difficult to detect. To address these challenges, Urosevic et al. (2011) implemented a monitoring program combining 3D vertical seismic profile (VSP) with 3D seismic data to increase the sensitivity of the time-lapse seismic analysis. Despite the challenges, subtle seismic anomalies were detected after injection of small quantities of CO_2-CH_4 mixture, and seismic modeling suggested that the prolonged injection is unlikely to produce detectable difference in time-lapse seismic analysis.

The in situ fluid in the pore space of the intended reservoir for CO_2 has significant impact on the applicability of time-lapse techniques for seismic monitoring, as seen in the

Otway project in Australia. In the Weyburn Field in Saskatchewan, Canada, within the Williston Basin CO_2 is injected for enhanced oil recovery (EOR) in a fractured carbonate reservoir. The carbonate reservoir is at a depth of approximately 1450 meters (White, 2009b). Rock physics and seismic modeling suggested a decrease of 3-6% of Vp when CO_2 replaced a mixture of oil and brine (Terrell et al., 2002; Meadows, 2013; White 2013b). In the case, of CO_2 replacing only brine the Vp changes 9-10% (White et al., 2004). This sensitivity to saturation of CO_2 makes time-lapse images good at mapping the movement of the injected CO_2 in the reservoir, but accurate volume estimation is difficult (Ma et al., 2009; White, 2009).

Other reservoir properties besides pore fluid can affect the efficiency of seismic methods to monitor injected CO_2 into the subsurface. In the Cranfield Field in Mississippi, CO_2 is injected into the cemented sandstones of the Tuscaloosa Formation, the depth of the reservoir is about 3020 to 3200 meters. Rock physics and seismic modeling suggested that due to the cement content in the sandstones of the Tuscaloosa Formation the seismic response presents small variability to different saturations of CO_2 difficult to detect in the seismic data (Carter and Spikes, 2013). However, statistical classification showed that elastic properties such as P-impedance and Vp/Vs are sensitive to CO_2 saturation, and lateral and time-dependent changes of these elastic properties permit the estimation of porosity and fluid saturation within the reservoir (Carter, 2014).

These various projects have demonstrated the valuable use of seismic methods in in CO_2 storage and EOR, with examples of successful monitoring of CO_2 injected into the subsurface. Seismic methods are equally essential for the characterization of a potential storage reservoir, determining the reservoir properties, and estimating its capacity. Different quantitative methods have been used to successfully estimate reservoir properties from seismic data, linking elastic parameters and reservoir properties. The work of Dvorkin

and Alkahater (2004), Dvorkin et al. (2004), Saltzer et al. (2005), and Bachrach (2006) are examples of the sequential workflow using seismic inversion followed by rock physics methods to estimate reservoir properties such as porosity, pore fluid and clay content. Seismic inversion is a commonly used technique that may help to map elastic properties like P-impedance, S-impedance, and density in the subsurface. However, the fundamental objective is to map reservoir properties such as porosity, clay content, and pore fluid. The rock physics models described by Mavko et al. (2009), Avseth et al., (2005), and Dvorkin et al., (2014) provide the quantitative link between elastic properties and reservoir properties.

As one of the most prolific hydrocarbon provinces and most heavily explored basin in the world, the Gulf of Mexico has incredible potential for CO_2 storage and EOR. The Miocene section of Texas Gulf of Mexico exhibits thick sand intervals with high porosity and permeability, effective trapping mechanism, and regional seals. To date, most of the offshore CCS research in the Gulf of Mexico has focused on subsurface storage capacity and reservoir flow simulations (Wallace, 2013), and structural aspects related to seal integrity (Nicholson, 2012; Osmond, 2016). These investigations have not identified any major geologic barriers to conducting large-scale CCS, so work continues to identify the regional and local capacity of the Miocene section, as well as identify specific sites suitable for near-term storage project development.

This study quantitatively evaluates the CO_2 storage capability of the Lower Miocene brine-filled sandstones in the inner continental shelf of the Texas Gulf of Mexico using 3D seismic and well log data. The first part of this work investigates the relationship between elastic properties and reservoir properties (e.g., porosity, mineralogy, and pore fluid) of the Lower Miocene section using rock physics modeling and simultaneous seismic inversion. The elastic properties are related to porosity, mineralogy and pore fluid using

rock physics models. These rock physics transforms are then applied to the seismically derived elastic properties to estimate the porosity and lithology away from the wells. The porosity and lithology distribution derived using this quantitative method can be interpreted to predict the best areas for CO_2 storage in the inner continental shelf of the Texas Gulf of Mexico. The second part of this work studies the effect that CO_2 has on the elastic properties of the Lower Miocene rocks using fluid substitution, amplitude variation with angle (AVA), and statistical classification to determine the ability of the seismic method to successfully monitor CO_2 injected into the subsurface. The velocities and density well logs were modeled with different fluid saturations. To characterize the seismic properties corresponding to these different fluid saturations, the AVA responses and probability density functions were calculated and used for statistical classification. The AVA modeling shows a high sensitivity to CO_2 due to the soft clastic framework of the Lower Miocene sandstones. The statistical classification successfully discriminates between brine and CO_2 saturation using Vp/Vs and P-impedance. These results shows that the Lower Miocene sandstone have the capacity to host CO_2, and that the CO_2 injected in these rocks is likely to be successfully monitored using seismic methods.

1.2 THESIS OUTLINE

Chapter 2 introduces the study area and the data used in this thesis. In this chapter, the stratigraphic and structural framework on the offshore areas of the Texas Gulf of Mexico are reviewed. Chapter 2 also describes the dataset. The data includes a 3D post-stack seismic volume, three partial angle stack volumes, and well log data from three wells.

Chapter 3 presents a quantitative method to estimate reservoir properties useful to characterize potential reservoirs for CO_2 storage. This method uses rock physics modeling

and seismic inversion to estimate porosity and lithology of the Lower Miocene section. First, a rock physics model is used to link elastic properties to porosity and mineralogy. Later, in this chapter is shown how a combination of elastic properties (Vp/Vs and P-impedance) can be used to map the spatial distribution sand and shales and calculate the porosity across the study area.

Chapter 4 examines how the elastic properties of the Lower Miocene sandstones are affected by different saturations of CO_2. This is done combining rock physics modeling, fluid substitution, amplitude variation with angle (AVA) modeling, and statistical classification. The results from this chapter show that due to the high porosity and soft frame of the sandstones the injected CO_2 significantly affects the elastic properties of the rock. In addition, using AVA modeling and statistical classification was identified that P-impedance and Vp/Vs are the elastic parameters that best discriminate between the different saturations of CO_2.

Chapter 5 discusses the overall conclusions drawn from the previous chapters and makes recommendations for future work.

Chapter 2: Study Area and Dataset

This chapter introduces the study area and the data used in this thesis. First, the geologic background of the Northern Gulf of Mexico is described, emphasizing the stratigraphic and structural framework of the Miocene section. Then, the available data that were used in this study is presented. The focus of this work is the Lower Miocene section in the near offshore areas of the Texas Gulf of Mexico. The available data include a 3D post-stack seismic volume, three partial angle-stacks and well logs from three different wells within the area covered by the seismic data.

2.1 Geologic Background

2.1.1 Stratigraphic Framework

The formation of the Gulf of Mexico basin began during the Mesozoic breakup of Pangea, by an episode of crustal extension and sea-floor spreading where the North American Plate began separating from the South American and the African Plate (Salvador, 1987; Sawyer et al., 1991; Buffler and Thomas, 1994). During the middle Jurassic initial breakup created a shallow basin (Galloway, 2001), where flooding alternated with periods of evaporation to produce widespread salt deposits (Louann Salt) (Salvador, 1987; Dobson and Buffler, 1997). The late Jurassic is characterized by seafloor spreading in the central Gulf of Mexico (Pilger, 1978; Hall et al., 1982; Buffler, 1989; Buffler and Sawyer, 1985; Sawyer et al., 1991). Deep water sediments were deposited on the newly formed oceanic crust, while shallow to deep water shelf environments were established on the broad areas of the adjacent transitional crust. (Buffler and Sawyer, 1985; Buffler 1991).

During the early Cretaceous, the Gulf of Mexico basin began to subside due to cooling of the lithosphere (Bluffer and Sawyer. 1985), and transgression onto the stable basin margin developed a carbonate platform around the periphery of the basin (Buffler and Sawyer, 1985; Winker and Buffler, 1988; Mcfarlan and Menes, 1991). Carbonate production ceased as rapid basinwide flooding drowned the early Cretaceous margin (Faust, 1990; Salvador, 1991).

The Laramide uplift that began in the Central and Southern Rocky Mountains and spread progressively south to the Sierra Madre Oriental of northern Mexico, during the Early Cretaceous and Early Eocene, provided a tremendous supply of clastic sediment into the Gulf of Mexico (Winker, 1982; Galloway, 2005b). This uplift resulted in a massive deposition of clastic sediments in the Gulf of Mexico, the high sediment volume accumulation rates caused the progradation of the continental margin by tens of kilometers (Galloway et al., 2000). Clastic deposition continued throughout the Oligocene followed by a large transgression that resulted in the deposition of the Anahuac Shale, marking the beginning of the Miocene interval.

Miocene basin fill is defined by three depositional episodes (Figure 2.1; Lower Miocene, Middle Miocene and Upper Miocene), and is characterized by extensive continental margin progradation (Figure 2.2) (Galloway, 2008). These depositional episodes are divided by extensive marine shale wedges that formed during a base-level rise that serve as markers for establishing a regional biostratigraphic correlation (Morton et al.,1988)

The Lower Miocene succession consists of an 8 Ma depositional episode that has been subdivided into two units, the Lower Miocene 1 (LM 1) and the Lower Miocene 2 (LM 2). These two units are separated by a regional transgressive shale containing *Marginulina ascensionensis* (*Marg*. A) fauna (Galloway, 2008). The Lower Miocene 1

corresponds to the Oakville sandstones of the shallow subsurface (inland) and to the dominantly progradational deposits at depth (offshore). The Lower Miocene 2 consist of the dominantly agraddational fluvial and retragradtioinal coastal deposits (Galloway et al., 1986). The Lower Miocene deposits are capped by the *Amphistenia* shale and the associated maximum flooding surface, which is named for the *Amphistegina chipolensis* (*Amph*. B) faunal top. The middle Miocene sequence records a relatively brief (ca. 3 m.y) period of deposition (Galloway, 2008) and corresponds to progradational deposits that record the advancement of the shelf margin. The Middle Miocene progradatinal deposits are capped by the regionally extensive *Textularina stapperi* (Text W) marine shale.

The upper Miocene depositional episode records a long period (6Ma) of relative paleo-geographic stability and high sediment supply when the Paleo-Mississippi and Paleo-Tennessee systems dominated the sediment input forming a fluvial dominated delta system that prograded onto the slope. In the central gulf margin offlap occurred and the shelf edge advanced 40-90 Km (Figure 2.2) (Galloway, 2008). The upper Miocene episode terminated with regional marine flooding associated with the last occurrence of benthic foraminifer *Robulus* E and/or *Bigenerina* A.

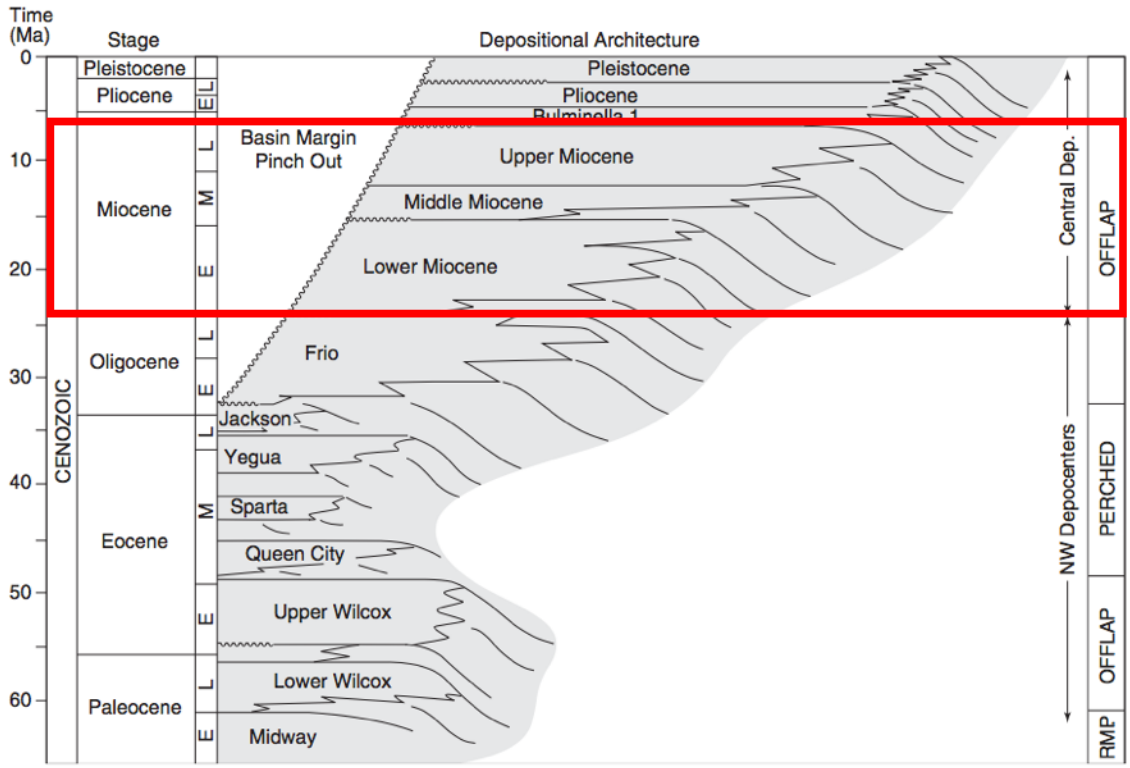

Figure 2.1: Generalized Cenozoic stratigraphic succession and architecture of the Northern Gulf of Mexico Basin. The Miocene deposits; Lower Miocene, Middle Miocene and Upper Miocene are highlighted by the red box. Modified from Galloway (2008).

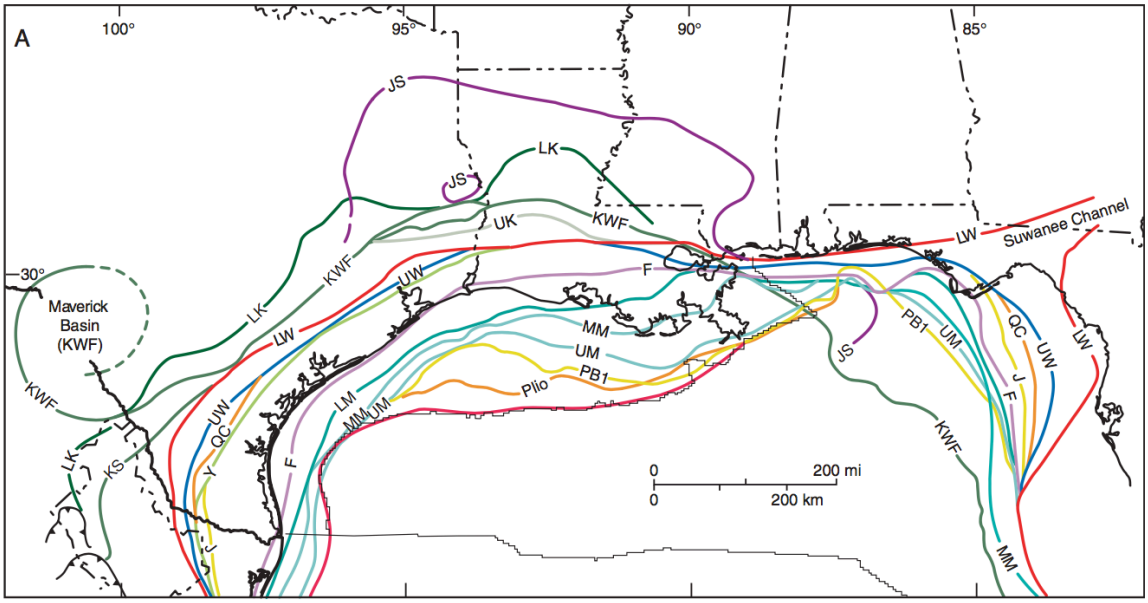

Figure 2.2: Mesozoic and Cenozoic shelf margins of principal depositional episodes in the Northern Gulf of Mexico. Showing the shelf margins progradation during the evolution of the basin. The Lower Miocene (LM), Middle Miocene (MM), and Upper Miocene (UM) are represented by the cyan lines. From Galloway (2008)

2.1.2 Structural framework

Miocene and post Miocene structural features are products of reactivation of older structures or contemporaneous structures initiated or accelerated by continental margin progradation (Winker, 1982; Winker and Edwards, 1983). These structures are manifested as large regional growth faults and as shale diapirs and shale ridges formed by vertical extrusion of highly mobile shelf-slope mudstones. The normal faults and shale ridges are generally orientated northeast-southeast that is closely the same orientation of the lower and middle Upper Miocene shelf margins.

Reactivated structures were initiated by shelf margin progradation and sedimentary loading during the earlier Cenozoic depositional cycles, and extensive deep and shallow salt diapirs that extend throughout the Houston salt basin. Salt diapirs of the inner and

middle shelf in the High Island and Galveston areas were likely mobilized by Miocene slope progradation. Reactivated faults typically have high angle and low expansion ratios; nevertheless, stratigraphic offset of younger sediments can be substantial (Galloway et al., 1986).

As is typical of actively prograding, terrigenous divergent margins (Winker and Edwards, 1983) and particularly in the Cenozoic Gulf coast continental margin (Jackson and Galloway, 1984), the lower Miocene deposits that built out beyond the underlying Frio continental platform initiated large-scale growth faulting and deep-seated sediment extrusion and uplift. The over-steepened gradient and low sediment strength create slope instabilities that promote detachment and downward rotation of huge fault blocks. Faults have down to the basin displacement that cause abrupt increase of stratigraphic thickness on the downthrown side (Galloway, 2008).

Figure 2.3 shows a strike-orientated seismic cross-section within the study area. The stratigraphic units interpreted in this figure are the Upper Miocene (UM), Middle Miocene (MM), the regional transgressive *Amphistenia* shale, Lower Miocene 1 (LM1) and Lower Miocene 2 (LM2) with the *Marginulina* shale that separates these two units. The stratigraphic units deposited during the Miocene are highly affected by the normal faulting in the area. These can affect the potential of CO_2 storage in the area, where the faults can create migration pathways, where the CO_2 can leak. However, these structures can provide structural traps that could be used for CO_2 storage.

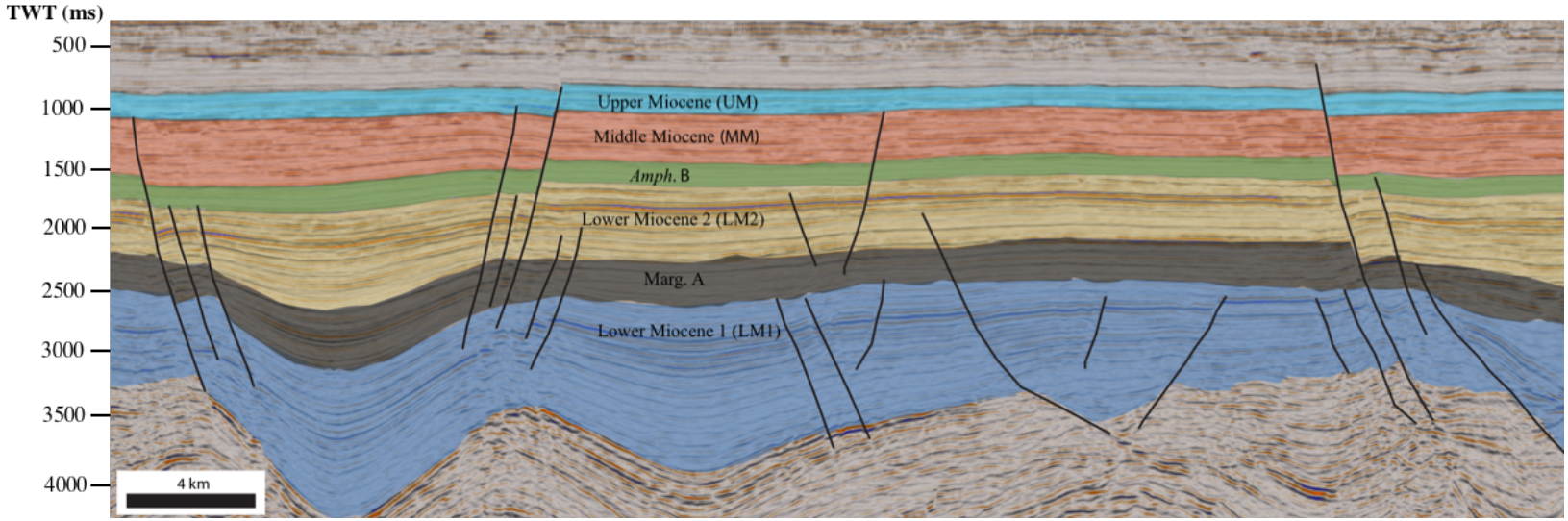

Figure 2.3: Strike–oriented seismic cross-section interpreted showing the structural style of the study are and the stratigraphic units. The interpreted units include the Upper Miocene (UM), Middle Miocene (MM), *Amph*. B shale, Lower Miocene 2 (LM2; focus of this study as a intended reservoir for CO_2 storage), *Marg*. A shale, and Lower Miocene 1 (LM1)

2.2 DATASET

The dataset used in this study is comprised of a 3D post-stack seismic volume, three partial angle-stack volumes (near-angle stack, mid-angle stack, and far-angle stack), and three wells (referred as well OCS 511, well OCS 518, and well OCS G6142). The seismic and well data is located in the coastal area of the Texas Gulf of Mexico (Figure 2.4).

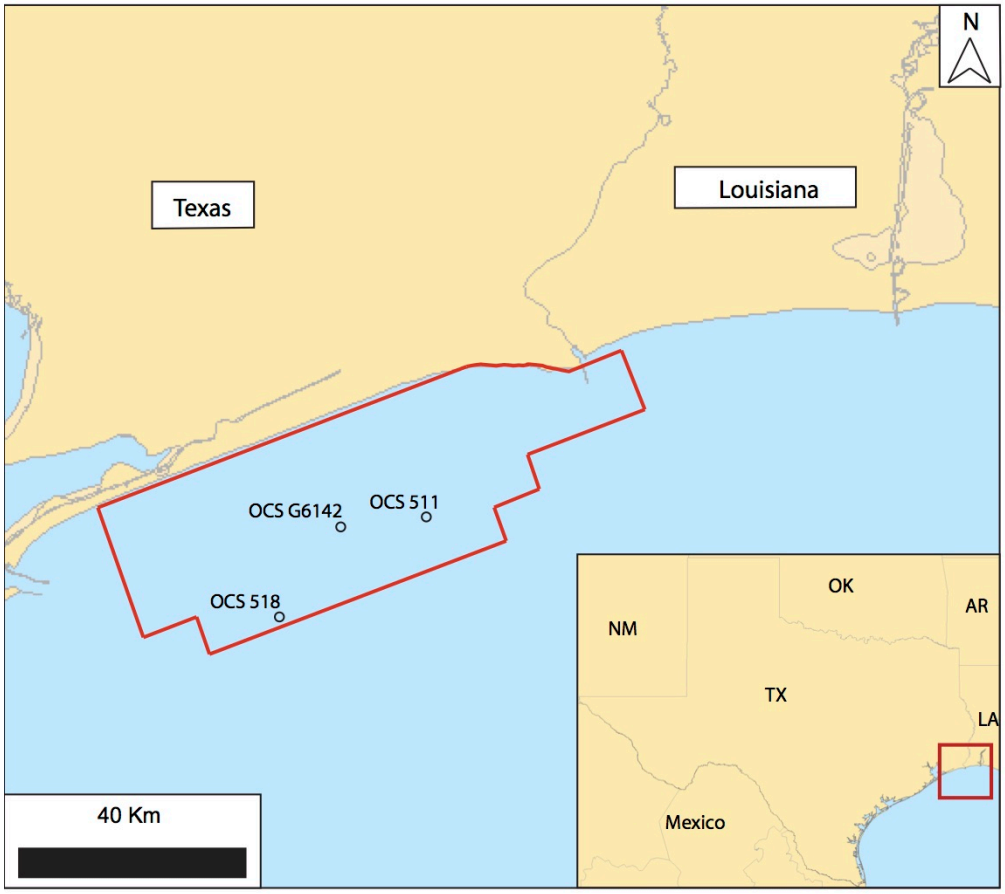

Figure 2.4: Map of the study area showing the location of the 3D seismic data and the location of the wells used in this study. The red box represents the area covered by the 3D seismic data and the circles the location of the wells.

2.2.1 Post-stack seismic data

The 3D post-stack seismic data cover a total area of 1206.60 mi^2, with an inline range from 5000-8700 and a crossline range from 5000-7200 spaced 110 ft. Figure 2.5 shows the amplitude spectrum of the 3D seismic data; the dominant frequency of the survey is 25 Hz range. Assuming an average P-wave velocity (Vp) of 2.7 km/s, the wavelength would be about 108 meters. Therefore, the vertical resolution of the seismic data, one fourth of the wavelength, is about 27 meters. Because the well data is displayed in feet, our seismic resolution in feet would be about 88 feet.

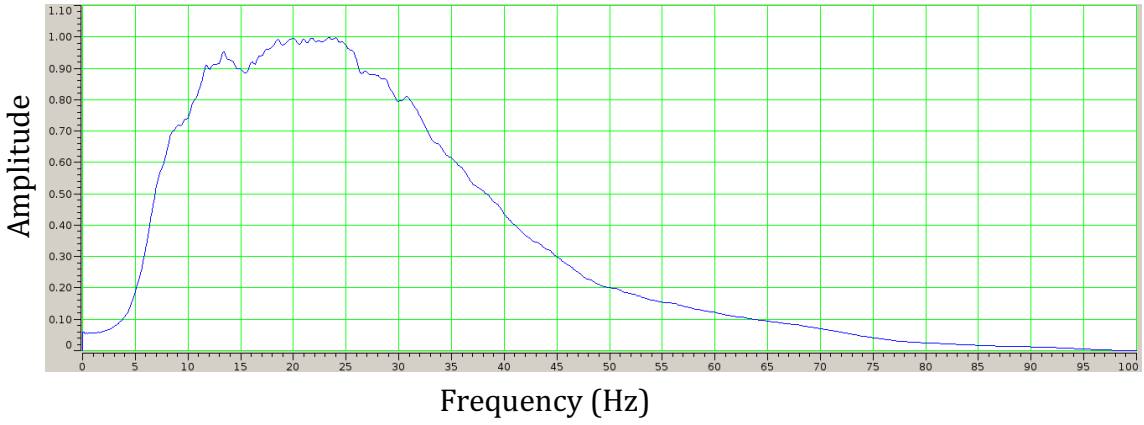

Figure 2.5: Amplitude spectrum of the 3D seismic data showing a dominant frequency between 18 to 25 Hz. The vertical axis is amplitude, and the horizontal axis is frequency in Hertz (Hz).

2.2.2 Partial angle stacks seismic data

The three partial angle-stack volumes (near, mid, and far) have the same geometry as described above for the 3D post-stack seismic data. The near angle stack volume is generated with angles between 0 to 14 degrees, the mid angle stack with angles from 14 to 27 degrees, and the far angle stack is generated with angles from 27 to 45 degrees.

2.2.3 Well log data

Logs from well OCS 511, well OCS 518 and well OCS G6142 in the coastal areas of the Texas Gulf of Mexico were used in this study. The relative location of each well within the seismic volume is shown in Figure 2.4. Table 2.1 shows the logs available at each well and Figures 2.6, 2.7, and 2.8 shows the logs of each well in the Lower Miocene section, where the black line in each figure represent the top of the Lower Miocene 2 (LM2).

Well\Logs	GR	ILD	NPHI	Density	Vp	Vs
OCS 518	X	X	X	X	X	
OCS 511	X	X	X	X	X	X
OCS G6142	X	X		X	X	

Table 2.1: Logs available for each well

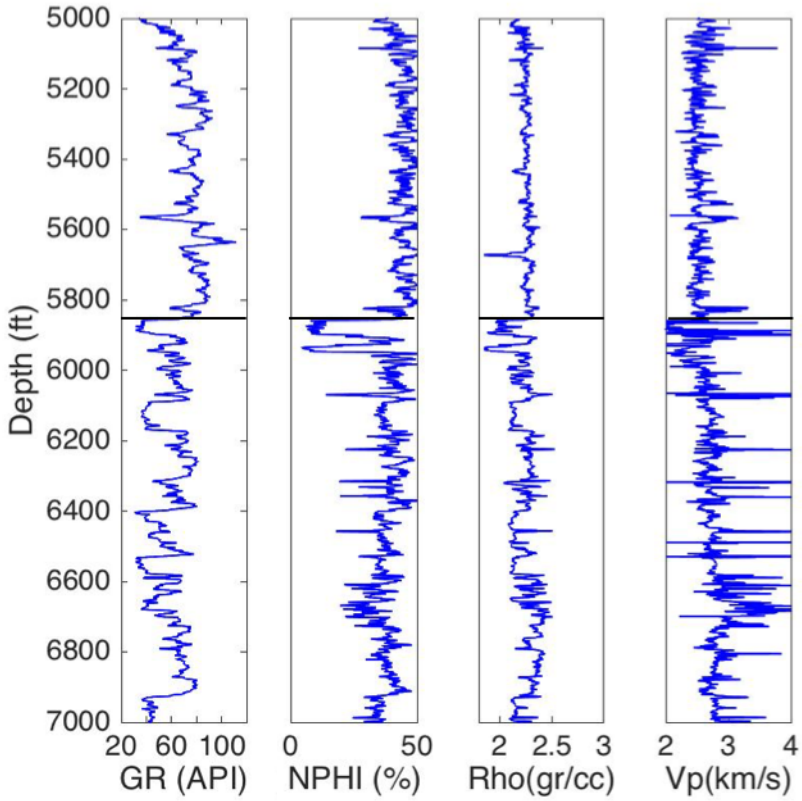

Figure 2.6: Well logs from well OCS 518. From left to right the well logs are gamma ray (GR), neutron porosity (NPHI), bulk density, and P-wave velocity. The horizontal black lines represent the top of the Lower Miocene 2 (LM2) sandstones.

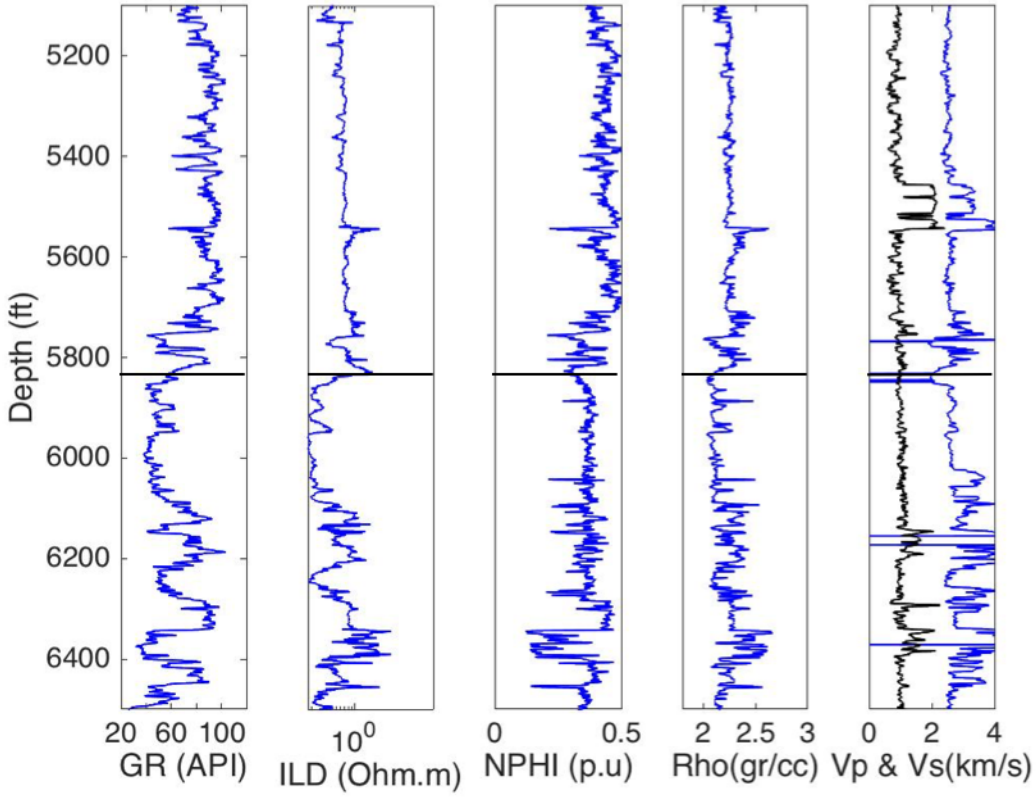

Figure 2.7: Well logs from well OCS 511. From left to right the well logs are gamma ray (GR), deep resistivity (ILD), neutron porosity (NPHI), bulk density, P-wave velocity and S-wave velocity. The black line represents the top of the Lower Miocene 2 (LM2) sandstones.

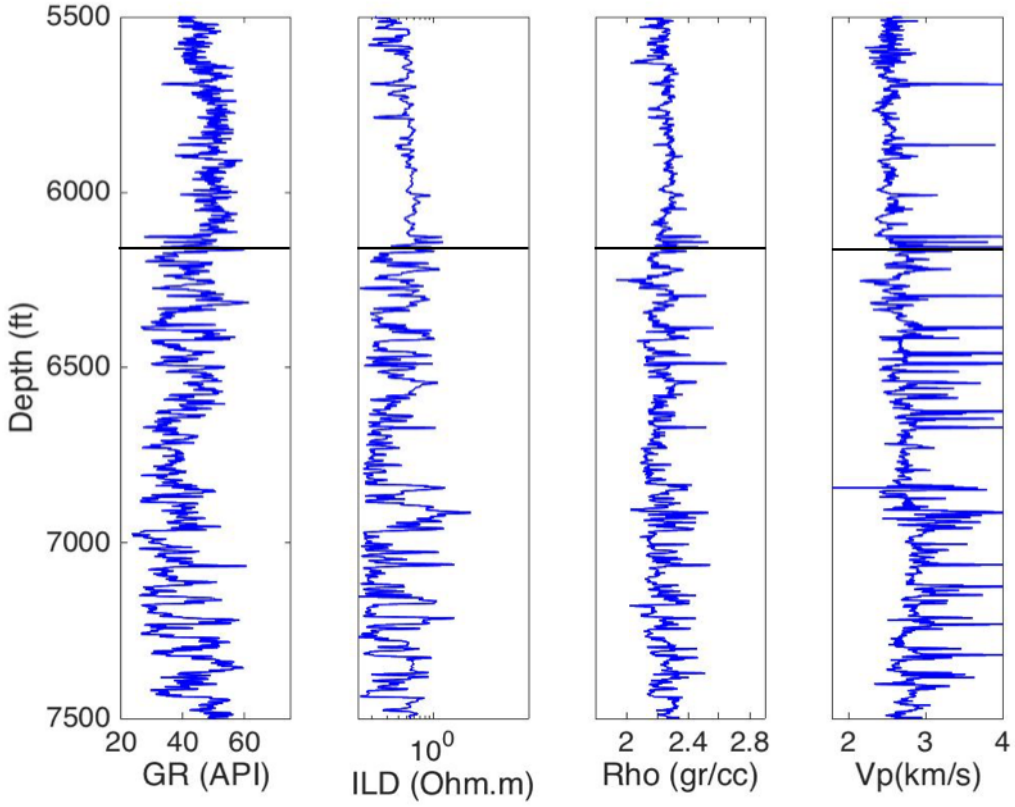

Figure 2.8: Well logs from well OCS G6142. From left to right the well logs are gamma ray (GR), deep resisitivity (ILD), bulk density, and P-wave velocity. The black lines represent the top of the Lower Miocene 2 (LM2).

Chapter 3: Porosity estimation using rock physics models and seismic inversion

3.1 INTRODUCTION

The intended reservoirs for CO_2 storage require favorable geologic properties such as high porosity and permeability, high seal capacity, and an effective trapping mechanism. Different quantitative methods have been used to successfully estimate reservoir properties such as porosity, mineralogy, and pore fluid from seismic data. These quantitative methods can be used for the characterization of potential storage reservoir, and estimating its capacity. Seismic inversion is a commonly used technique that may help to map elastic properties like P-impedance, S-impedance, and density in the subsurface. However, the fundamental objective is to map reservoir properties such as porosity, clay content, and pore fluid. Using rock physics models the elastic properties can be related to porosity, mineralogy, and pore fluid. In principle, such transforms can be applied to the seismically derived elastic properties to determine the rock properties in the subsurface.

The work of Dvorkin and Alkahater (2004), Dvorkin et al. (2004), Saltzer et al. (2005), Bachrach (2006) are examples of the sequential workflow using seismic inversion followed by rock physics modeling to estimate reservoir properties. Dvorkin and Alkahater (2004) used rock physics to map pore fluid and porosity from seismic data. Showing that combining model-based rock physics analysis with seismic data it is possible to discriminate gas-saturated intervals from liquid-saturated intervals using P-wave data. Saltzer et al. (2005) used successfully a cascaded seismic and rock physics inversion workflow to estimate porosity and volume concentration of shale. The workflow consisted in two steps: (1) a simultaneous inversion of angle-stacks to obtain P-impedance and S-

impedance, (2) the next step is to convert the impedances derived from the first step to lithology and porosity values using a rock physics model.

This chapter combines rock physics modeling and simultaneous seismic inversion to estimate the porosity and lithology of the Lower Miocene section in the inner continental shelf of the Texas Gulf of Mexico, which are at a depth between 5500 and 6200 feet. Using well log data, the soft-sand model (Dvorkin and Nur, 1996) is calibrated to link the elastic properties of the Lower Miocene section to the rock properties. Then, a pre-stack seismic inversion is performed to obtain elastic properties of the subsurface from the seismic data. The goal of this chapter is to apply the rock physics transforms, calibrated with the well log data, to the seismic-impedance inversion data to map lithology and porosity. The scales of the seismic data are much larger than the scale of the well log data. To address this issue, the well log data are upscaled using the Backus (1962) average, and then the rock physics transforms are applied to the seismically derived elastic properties to calculate the porosity and predict the lithology away from the wells in the Lower Miocene section. The results appear to be accurate when compared to well log data.

3.2 METHODOLOGY

The methods used in this chapter integrate rock physics modeling and simultaneous seismic inversion. The main steps used in this chapter are (1) select a rock physics model and calibrate the rock physics model with well log data, (2) discriminate between sand and shales combining Vp/Vs and P-impedance, (3) upscale the well log data to the seismic scale, (4) perform pre-stack seismic inversion, and (5) use Ip-porosity equations to derive porosity from the seismic inversion.

For this study the three partial-angle stacks (near, mid, and far) were used with the geophysical logs from the wells OCS 511, OCS 518, and OCS G6142. The well OCS 511 and OCS 518 were used in the rock physics modeling and as training data for the simultaneous seismic inversion, while well OCS G6142 was used as a test well.

3.2.1 Rock Physics Model

Rock physics models are used to characterize, understand, and quantify the impact of specific reservoir properties (e.g., lithology, porosity, pore fluids, clay content) on the elastic properties. Example of different rock physics models are described by Mavko et al. (2009), Avseth et al. (2005), and Dvorkin et al. (2014). These different rock physics models can be based on theoretical models or in empirical relations, and may describe different geologic scenarios. Therefore, it is important to take into account the geologic nature of the sediments when selecting a rock physics model.

For this study, the soft sand model (Dvorkin and Nur, 1996) was used. The soft sand model (or friable sand model) can be used to calculate the elastic moduli of well-sorted and poorly-sorted soft sands. The starting point of the model is to calculate the elastic moduli of a well sorted, high porosity sand using the Hertz-Mindlin contact theory (Mindlin, 1949). The Hertz- Mindlin contact theory (Mindlin, 1949) can be use to describe the properties of precompacted granular rocks, and gives the following expressions for the effective bulk and shear moduli of a dry, dense, random pack of identical spherical grains subject to hydrostatic pressure P:

$$K_{HM} = \left[\frac{C^2(1-\phi_C)^2\mu^2}{18\pi^2(1-\upsilon)^2}P\right]^{1/3}, \tag{3.1}$$

$$\mu_{HM} = \frac{5 - 4\upsilon}{5(2 - \upsilon)}\left[\frac{3C^2(1 - \phi_C)^2\mu^2}{2\pi^2(1 - \upsilon)^2}P\right]^{1/3}, \tag{3.2}$$

where ϕ_C is the critical porosity, C is the coordination number, μ and υ are the mineral shear modulus and Poisson's ration.

The effective elastic moduli of sand with porosities between 0 and critical porosity are interpolated using the lower Hashin–Shtrikman bound. The effective moduli (K_{eff} and μ_{eff}) are calculated using the following expressions:

$$K_{\text{eff}} = \left[\frac{\phi/\phi_C}{K_{HM} + \frac{4}{3}\mu_{HM}} + \frac{1 - \phi/\phi_C}{K + \frac{4}{3}\mu_{HM}}\right]^{-1} - \frac{4}{3}\mu_{HM}, \tag{3.3}$$

$$\mu_{\text{eff}} = \left[\frac{\frac{\phi}{\phi_C}}{\mu_{HM} + \frac{\mu_{HM}}{6}\left(\frac{9K_{HM}+8\mu_{HM}}{K_{HM}+2\mu_{HM}}\right)} + \frac{1 - \frac{\phi}{\phi_C}}{\mu + \frac{\mu_{HM}}{6}\left(\frac{9K_{HM}+8\mu_{HM}}{K_{HM}+2\mu_{HM}}\right)}\right]^{-1} - \frac{\mu_{HM}}{6}\left(\frac{9K_{HM} + 8\mu_{HM}}{K_{HM} + 2\mu_{HM}}\right). \tag{3.4}$$

To construct the rock physics models was assumed, for simplicity that the only minerals present in the rock are clay and quartz. To compute the effective mineral moduli for a mixture of clay and quartz the Voigt-Reuss-Hill average is used (Mavko et al. 2009).

For wells OCS 518 and OCS G6142, no S-wave velocity curves are available. To calculate the S-wave velocity for these wells, the Castagna et al. (1985) mudrock equation was used:

$$V_s = 0.862V_p - 1.172\,. \tag{3.5}$$

3.2.1.1 Rock physics model calibration to well log data

The next step is to validate the applicability of the model selected by calibrating the rock physics model with the well log data. Using the measured velocity and density at the well, and the total porosity calculated from the density log using the following formula:

$$\phi = \frac{\rho_m - \rho_b}{\rho_m - \rho_f}, \tag{3.6}$$

where ρ_f is the density of the fluid in the pore space, ρ_b is the bulk density measured at the well, and ρ_m is the density of the matrix.

The P-impedance in the Lower Miocene 2 (LM2) interval is plotted versus the porosity in Figure 3.1 for well OCS 518 and Figure 3.2 for well OCS 511. It is color-coded by gamma ray value. The P-impedance-porosity curves drawn from the soft sand model (section 3.2.1) are superimposed with the data points. These theoretical curves from the soft sand model are calculated for 100% water saturation, and constant clay content at 25% increments. The high-porosity end member used was the critical porosity for sandstone of 39%. The mineral and fluid properties used are from Table 3.1.

Fluid/Mineral	Bulk Modulus (GPa)	Shear Modulus (GPa)	Density(g/cc)
Quartz	37	44	2.65
Clay	25	9	2.55
Brine	2.73	0	1.033
CO_2	0.0871	0	0.691

Table 3.1: Fluid and mineral properties used in rock physics modeling and fluid substitution analysis. The elastic properties of the fluids are obtained using the Batzle-Wang equation. The elastic properties of the minerals used are from Mavko et al. (2009).

The soft sand model curves for P-impedance and porosity calculated for different clay content and 100% brine saturation accurately match the data for wells OCS 518 and OCS 511 in Figure 3.1 and Figure 3.2, which shows the utility of the model selected here. The model based impedance-porosity curves drawn for pure quartz sand and sand with 25% clay bound the sand data points. Model based impedance-porosity curves are also drawn for rock with 50%, 75%, and 100% clay content. Most of the shale data lies between the 50% and 75% clay content curves, which means that the shale is not pure clay.

The selection of the rock physics model is based on the geological nature of the Lower Miocene 2 (LM2) section in the upper Texas Gulf of Mexico. The match between the well log data and the rock physics model demonstrates the consistency of the geological setting and the soft sand model (Figures 3.1 and 3.2). From Figures 3.1 and 3.2 can be observed that both porosity and clay content (gamma ray) affect the P-impedance. At a constant percentage of clay (gamma ray), low porosity corresponds to a large P-impedance, whereas at a fixed porosity increased percentage of clay (hotter colors) correspond to lower P-impedance.

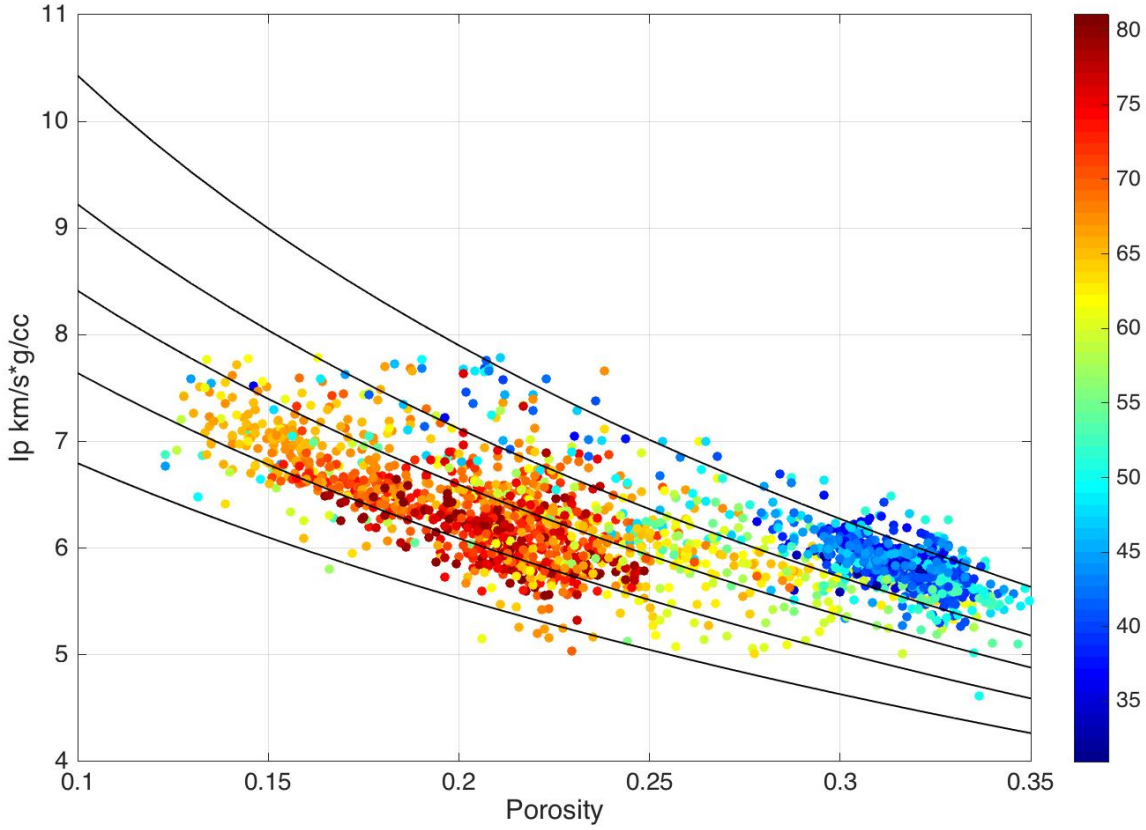

Figure 3.1: P-impedance plotted versus porosity for the Lower Miocene 2 (LM2) section of log data from well OCS 518. The data are color coded by gamma ray. The black curves are from the soft sand model, each drawn for a fixed clay content starting at 0% and ending at 100% clay, increasing 25% the clay content.

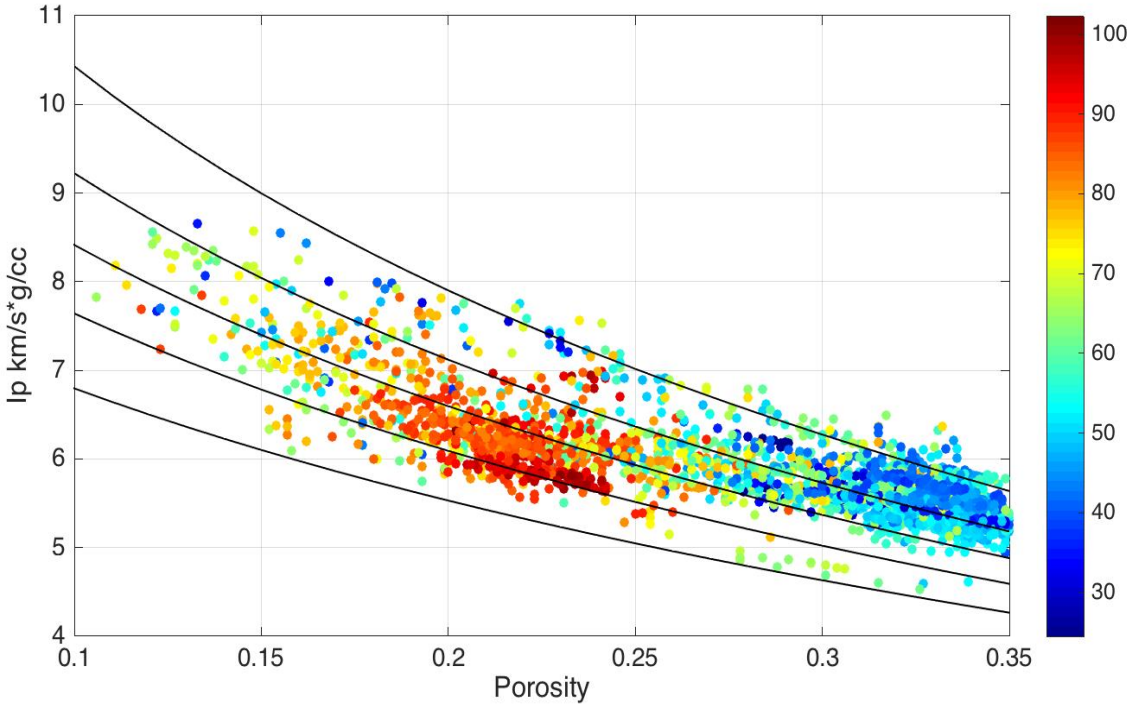

Figure 3.2: P-Impedance plotted versus porosity for the Lower Miocene 2 (LM2) section of log data from well OCS 511. The data are color coded by gamma ray. The black curves are from the soft sand model, each drawn for a fixed clay content starting at 0% and ending at 100% clay, increasing 25% the clay content.

3.2.2 Lithology discrimination and porosity estimation

Figure 3.3 shows the plot of Vp/Vs vs P-impedance for well OCS 518, color-coded by gamma ray. The well data displayed shows that the sand and shales do not overlap, which means, that the sands and shales can be identified by using a combination of P-impedance and Vp/Vs. To make this identification, a cut-off line was drawn below the shale domain that is represented in Figure 3.3 by the black line. The corresponding equation is:

$$V_p/V_s = 0.0047I_p^2 - 0.16I_p + 2.8. \tag{3.7}$$

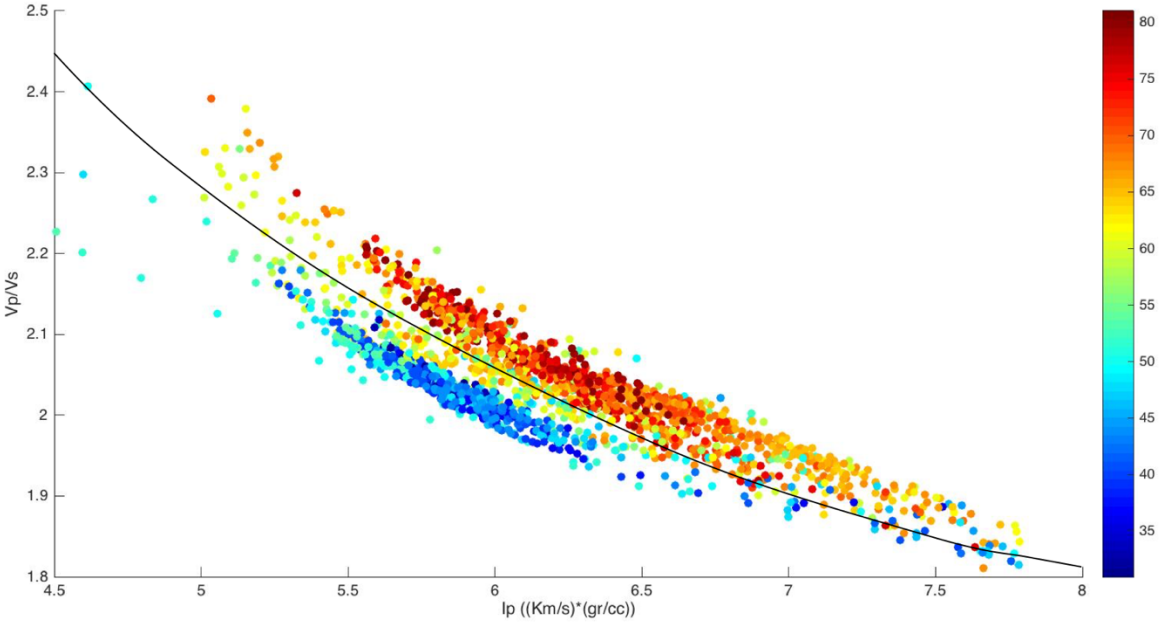

Figure 3.3: Vp/Vs plotted versus P-Impedance of the Lower Miocene section of log data from well OCS 518. The data are color coded by gamma ray. The black curve represents the cut off line between sands and shales.

If $V_p/V_s < 0.0047I_p^2 - 0.16I_p + 2.8$, then the domain is sand. If $V_p/V_s < 0.0047I_p^2 - 0.16I_p + 2.8$, then the rock is shale.

After discriminating between sands and shale using P-impedance and Vp/Vs, the porosity of the sands and shales can be estimated using the Ip-porosity transform from the rock physics model (section 3.2.1; Figs. 3.1 and 3.2). The plot of the Ip versus porosity in Figures 3.1 and Figure 3.2 indicates that the sand data (cooler colors) lies between the 0% clay and 25% clay line and that the shale data point (hotter colors) lies between the 50% and 75% clay content curves. Thus, the Ip- porosity transform for 15% clay was used to predict porosity from P-impedance, 65% clay line was used to predict the porosity in the shaley zones. The equation used to calculate the porosity for the sands is:

$$\phi = 0.0052Ip^2 - 0.1346Ip + 0.9067. \quad (3.8)$$

The equation used to estimate the porosity in the shaley zones is:

$$\phi = 0.0084Ip^2 - 0.19Ip + 1. \quad (3.9)$$

3.2.3 Upscaling

The shale-sand cut off criterion and the rock physics models are reasonably consistent with the log data. Due to the differences between the log-scale and seismic-scale the rock physics transforms should not be directly applied to the seismic data. In order to address this issue, the Backus (1962) average is applied to upscale the elastic moduli, and the arithmetic mean to upscale the bulk density and porosity; to evaluate if the rock physics transforms and cut off criterion are applicable at the seismic scale. The P-impedance at seismic scale is calculated from the upscaled moduli and density. The length of the window used is comparable with the seismic wavelength, approximately ¼ of the seismic wavelength, approximately 88 feet (Chapter 2; section 2.2.1)

Effective Density and Porosity:

The arithmetic mean of the porosity and density from the log data within the previously stated window are calculated using the following formulas (Rasolovoahangy, 2002):

$$\rho = \frac{1}{n}\sum_{i=1}^{n}\rho_i\,, \quad (3.10)$$

$$\phi = \frac{1}{n}\sum_{i=1}^{n} \phi_i \ , \tag{3.11}$$

where ϕ_i and ρ_i are the porosity and density at depth i, ρ and ϕ are the porosity and bulk density within the specified window, and *n* is the window size.

Effective Bulk and Shear Moduli:

To average the bulk and shear moduli within a given window using the Backus average.

$$< M >= \left(\frac{1}{n}\sum_{i=1}^{n}\frac{1}{M_i}\right)^{-1}, \tag{3.12}$$

where M_i are individual consecutive elastic modulus readings and <*M*> is the upscaled elastic modulus.

3.2.3.1 Upscaled results for the rock physics modeling

Figure 4.4 shows the crossplot of Vp/Vs and P-impedance upscaled at the seismic scale, color coded by gamma ray. The black dots represent the log data from the Lower Miocene 2 (LM2) section and the black line is the cutoff line for sands and shale given by equation 3.7 from Figure 3.3. Figure 3.5 shows the crossplot of the P-impedance and the porosity from well OCS 518, superimposed on the clay lines given by the soft sand model. The actual log values from the Lower Miocene section are in black, whereas the upscale values are color coded by gamma ray value. These figures demonstrate that the elastic properties of the upscaled log data can be characterized by the soft sand model, and proves

the possibility of discriminating between sands and shale, and estimate porosity from seismic data.

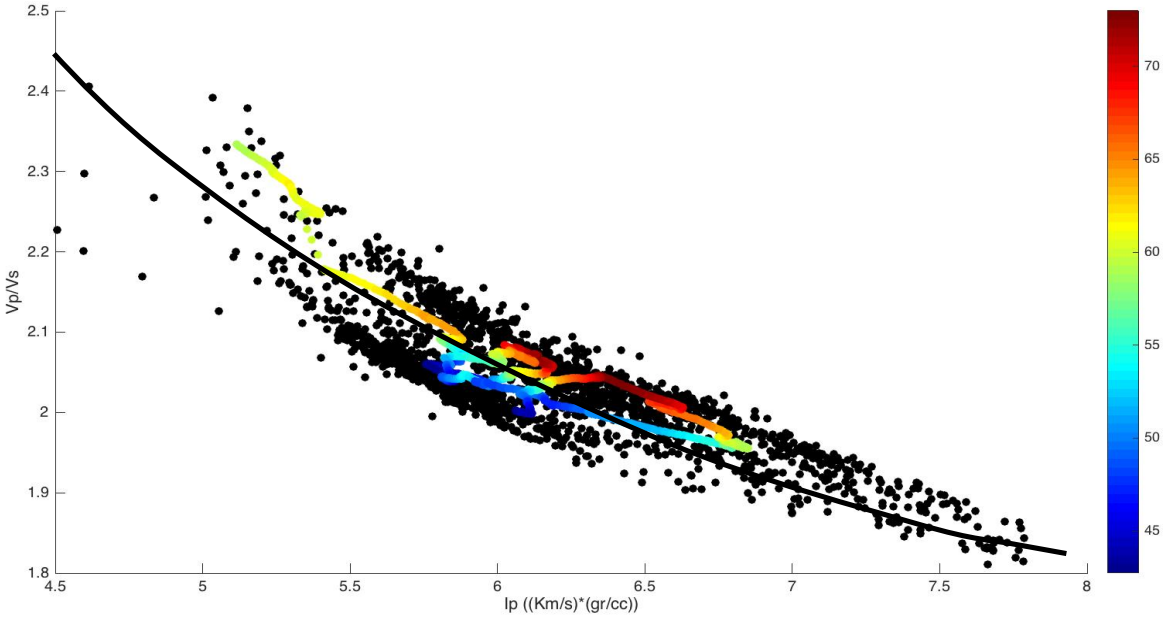

Figure 3.4: Vp/Vs plotted versus P-Impedance of the Lower Miocene section of the upscaled data from well OCS518 at the seismic scale. The data are color coded by gamma ray. The black curve represents the cut off line between sands and shales. The black dots represent the data from the well (compare with Figure 3.3).

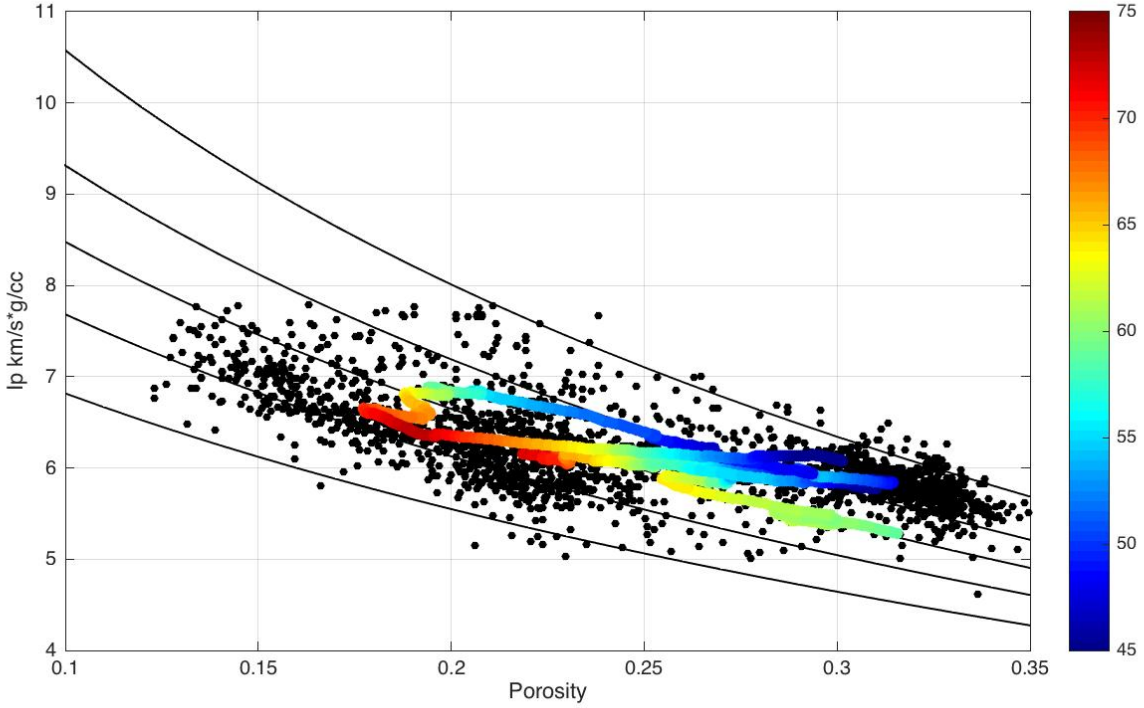

Figure 3.5: P-Impedance plotted versus porosity of the Lower Miocene section of the upscaled data from well OCS518 at the seismic scale. The data are color coded by gamma ray. The black curve represents the cut off line between sands and shales. The black dots represent the data from the well (compare with Figure 3.1)

3.2.4 Seismic inversion

To generate the P-impedance, S-impedance and density volumes, a simultaneous model-based inversion was performed using the Hampson-Russell© software. The algorithm used to perform the inversion assumes a linearized approximation for reflectivity, angle dependent reflectivity (Aki and Richards, 2002), and linear relationships among the logarithms of P-Impedance, S-Impedance, and density (Hampson et al., 2005). For this study, three partial angle-stacks were available; near angle-stack (angles up to 14 degrees), mid angle-stack (angles from 14 to 27 degrees), and far angle-stack (angles from 27 to 45 degrees). Figure 3.6 shows three different panels with each partial angle-stack.

The P-impedance log from wells OCS 518 and OCS G6142 are superimposed with the seismic data. The well OCS 518 was used in the well tie and as the training well for the model-based inversion, and the well OCS G6142 is the test well for the model-based inversion. A reasonable match between the inversion volumes and measured values in well OCS G6142 will be a good indication of the quality of the inversion results.

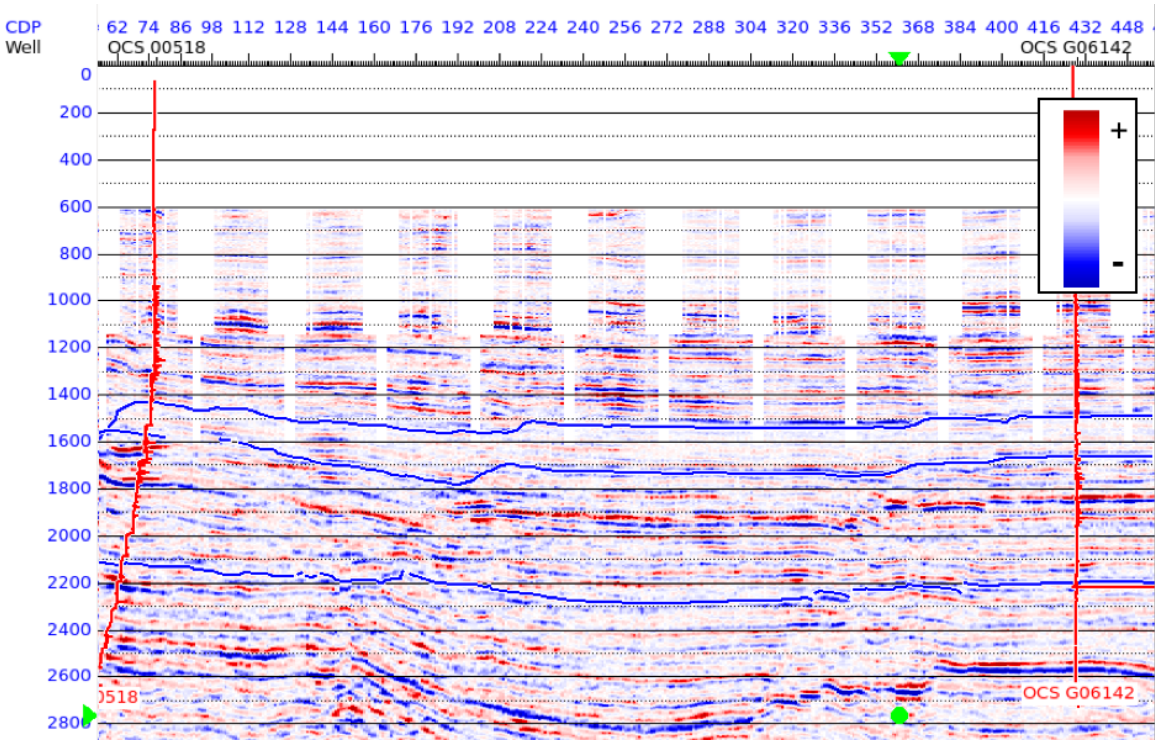

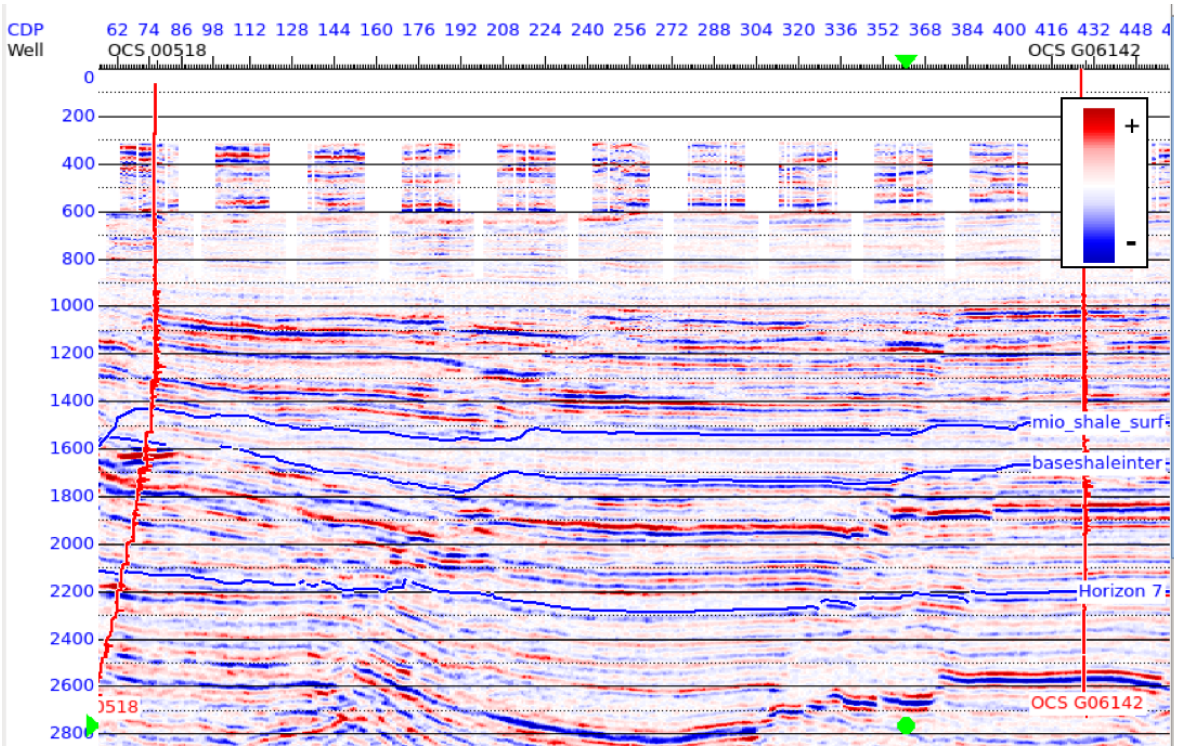
CDP
Well
OCS 00518
OCS G06142
mio_shale_surf
baseshaleinter
Horizon 7
OCS G06142

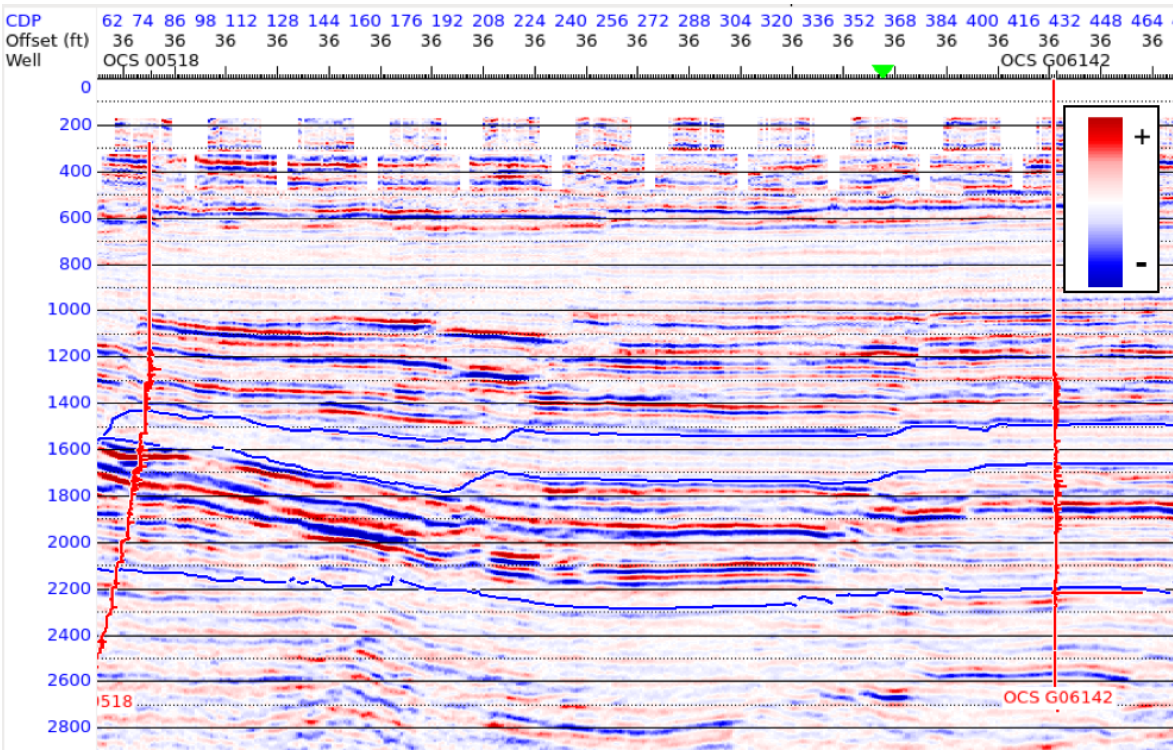
CDP
Offset (ft)
Well
OCS 00518
OCS G06142
OCS G06142

Figure 3.6: Arbitrary line connecting two wells in the study area of the three partial stacks available for this study. The upper panel shows the arbitrary line for the near partial stack with angles up to 14 degrees. The middle panel is the partial stacks of angles between 14 and 27 degrees. The lower panel is the arbitrary line of the far stack with angles from 27 to 45 degrees. The P impedance log is superimposed in all three sections for wells OCS 6142 and for well OCS 518.

Figure 3.7 shows the inversion analysis at well OCS 518 including from left to right the results for P-impedance, S-impedance, density and Vp/Vs. The black line represents the initial model, the blue line is the measured value at the well, and the red line is the inversion results at the well. Figure 3.7 also shows the wavelet group used in the inversion and the synthetic traces generated from the inverted model.

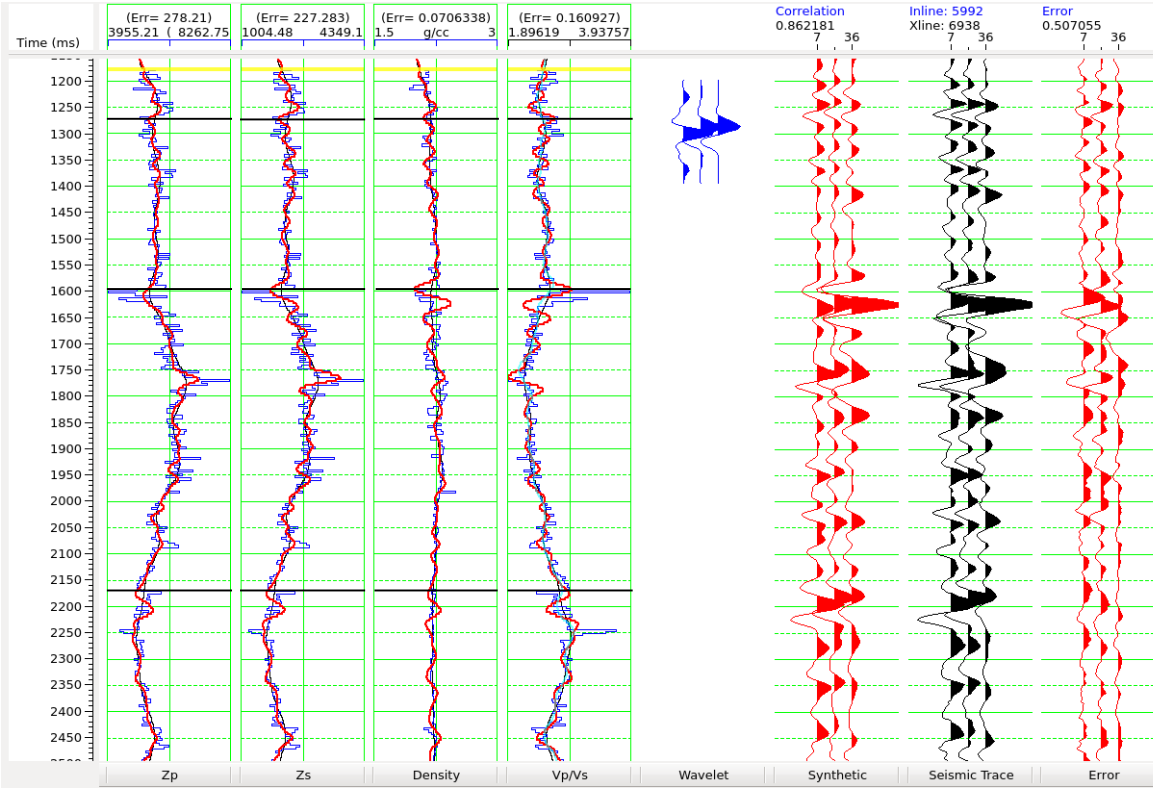

Figure 3.7: Inversion analysis window at well OCS 518, showing from left to right the inversion results for P-impedance, S-impedance, density, and Vp/Vs. The initial model is represented in black, the measured value at the well in blue, and the red is the inversion result at well OCS 518. The next panel is the wavelet group (blue) used in the inversion analysis and the synthetics seismic traces generated from the inverted model.

Figure 3.8 shows an arbitrary line through well OCS 518 and well OCS G6142 in three inverted volumes: P-impedance, S-impedance, and density respectively. The wells are superimposed showing the measured property obtain from the well logs, with the same color scale. It is important to highlight that the well OCS G6142 (right side) was not used in the seismic inversion and is used as a test well. The inversion results reasonably match the measured well data at the training well (OCS 518) and at the test well (OCS G6142) in the Lower Miocene section.

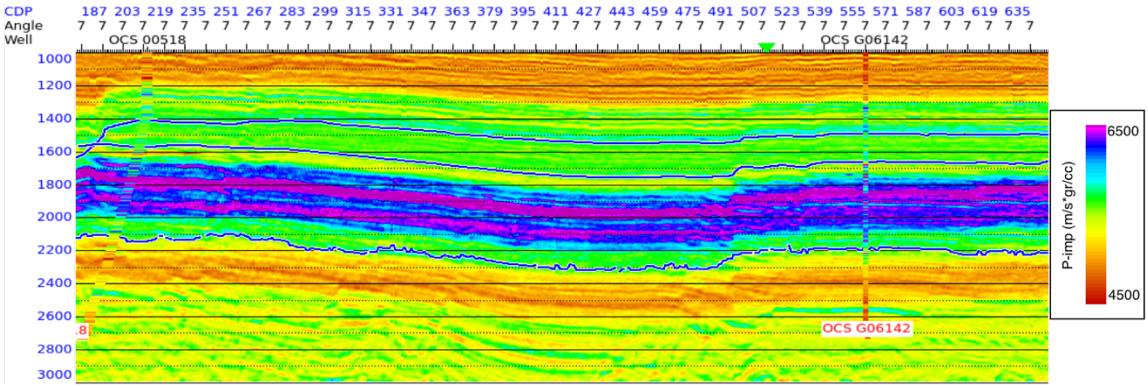
CDP
Angle
Well
OCS 00518
OCS G06142
P-imp (m/s*gr/cc)
6500
4500

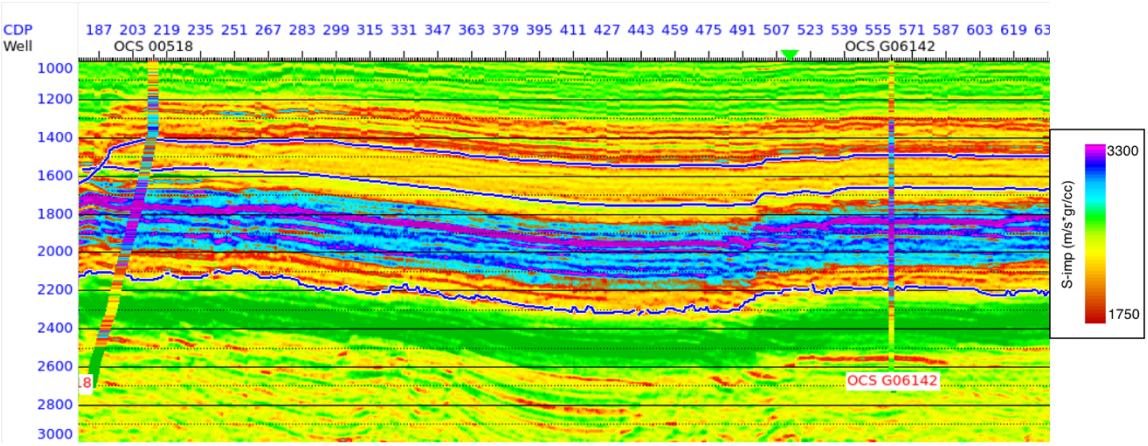
CDP
Well
OCS 00518
OCS G06142
S-imp (m/s*gr/cc)
3300
1750

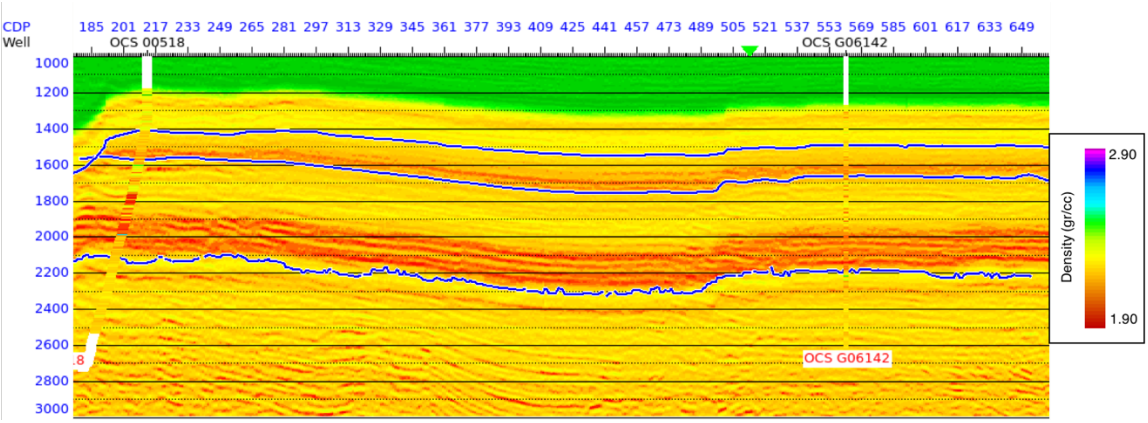
CDP
Well
OCS 00518
OCS G06142
Density (gr/cc)
2.90
1.90

Figure 3.8: Inversion results. Arbitrary line through both wells in all three inverted volumes in time color coded by the inverted property the three partial stacks available for this study. The upper panel shows the arbitrary line for the P-impedance. The middle panel is the S-impedance. The lower panel is the density volume. The values of each property at well OCS 511 and well OCS G6142 are superimposed in all three sections with the horizons interpreted in the seismic of the *Amph*. B shale and the Lower Miocene section.

3.3 Application of rock physics model to inversion results

In the previous sections (Section 3.2.3.1) was demonstrated that the elastic properties obtained from the seismic inversion can be used discriminate lithology and estimate porosity. Through the combination of the seismically derived Vp/Vs and P-impedance volumes, the sands and shales were delineated using the cut off line described by equation 3.7. Then, the porosity was estimated using equation 3.8 for sands and 3.9 for shales.

3.3.1 RESULTS

Using the properties obtained from the pre-stack seismic inversion (P impedance and Vp/Vs; Fig. 3.8) and the equations obtained from the rock physics models (eq. 3.7, 3.8, and 3.9), the lithologies and porosity can be broadly in the seismic data (Figure 3.9). Figure 3.9 shows an arbitrary line with the lithologies obtained from the rock physics model, and the porosity estimated by using the Ip-porosity transforms represented by equation 3.8 for sand intervals and equation 3.9 for the shaley zones. The wells OCS G6142 and OCS 518 are superimposed showing the sand and shales interval and the porosity at both wells.

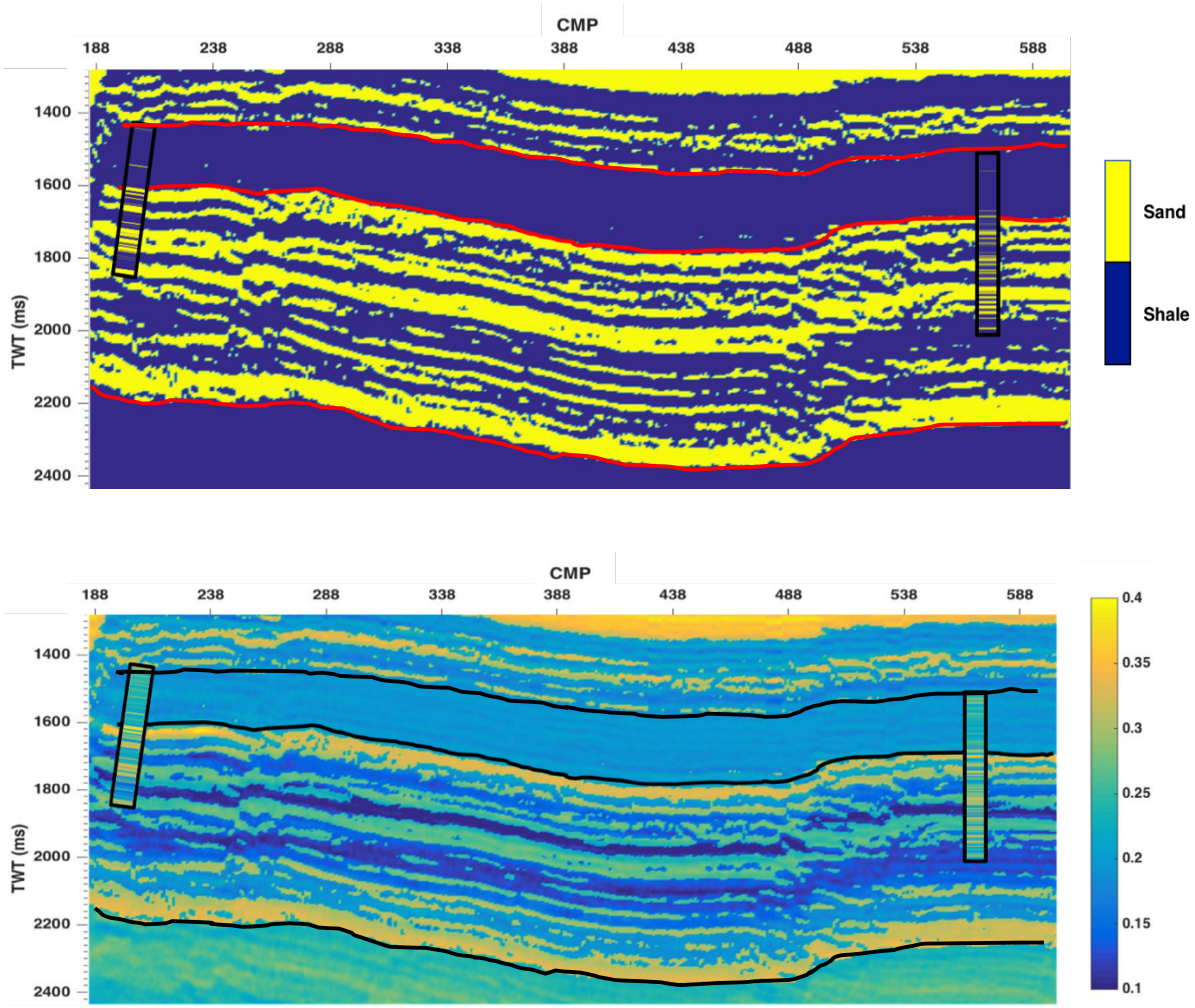

Figure 3.9: Arbitrary line showing the lithology and porosity estimated using the inversion results and the rock physics models. In the upper figure the yellow color represents the sands and the blue color the shales. In the lower figure the color represents the porosity obtained from the Ip-porosity transform from the rock physics models. The red lines in the upper figure and the black lines in the lower figure represents the top and base of the *Amph*. B shale and the Lower Miocene 2 (LM2).

The lithology and porosity results within the Lower Miocene 2 (LM2) interval match the measured data at the well. The well on the right (Figure 3.9), the OCS G6142 is a test well that was not used in the inversion. The sands delineated from the seismic data around well OCS G6242 shows to be thicker than the observed measures from the wells

(Figure 3.9). The reason is that the upscaled P-Impedance and Vp/Vs are not sensitive to the thin layers of shales that can be seen at the well log resolution. This means that some shaley zones are classified as sands and the porosity in these areas can be overestimated.

3.4 DISCUSSIONS AND CONCLUSIONS

Obtaining the porosity and lithology of the reservoir from elastic properties is relevant to several applications. Regarding CCS, it can be used to select more appropriate zones for CO_2 storage, calculate the capacity for intended reservoirs, and for flow simulation of future CO_2 injected. This work shows how to select and calibrate a rock physics model with well log data and also establish if this rock physics model can be used at the seismic scale.

The main intention of this work was to determine the effectiveness of workflows and methodologies that have been successfully applied in the oil and gas industry for characterizing reservoirs for CO_2 storage. In this work is demonstrated that this methodology can be used to obtain volumetrically continuous estimates of reservoir properties. Although not undertaking as part of the thesis research, these results could be the used for storage capacity estimation and CO_2 migration simulation, which might be preferable to extrapolating these properties from wells into statistically generated volumes.

Chapter 4: Sensitivity analysis of Lower Miocene sandstones to CO_2 saturation in the inner continental shelf of the Texas Gulf of Mexico.

4.1 INTRODUCTION

For CCS to be effective, the CO_2 should be monitored during and after injection to guarantee that it is safely retained underground. Among the monitoring methods for CO_2, the seismic methods provide the volumetric coverage needed to understand the spatial distribution of CO_2 in the subsurface (McKenna et al.; 2003; Lumley, 2010; Sava, 2013). Seismic methods have been used for monitoring CO_2 sequestration in different geological scenarios through time-lapse applications. Time-lapse seismic methods attempt to quantify the difference in the seismic response before and after the injection of CO_2 (Lumley, 2010; Dvorkin et al., 2014).

The stratigraphy of the Gulf of Mexico has a great potential for CO_2 storage. The basin has many extensive and thick sandstone reservoirs with high porosity (~ 30%) and high permeability (>1 darcy), thick regional shale intervals (seals), structural deformation from salt tectonism and growth faulting that has created numerous effective traps, (Nicholson, 2012; Osmond, 2016), and proximity to multiple point sources of high CO_2 emissions along the Texas coast (Wallace, 2013). Despite the potential of the basin for CO_2 storage, few studies have focused on understanding how injected CO_2 could affect the elastic properties of the saline aquifers that could be used for storage, and quantify the ability of the seismic methods to monitor the migration of the CO_2 into the formation

This chapter assesses the sensitivity of seismic P-wave velocities and PP reflectivity on CO_2 saturation that might result from injection and migration. The approach uses well log data and integrates rock physics modeling, fluid substitution, amplitude variation with

angle (AVA), and statistical classification to discriminate between brine and CO_2 saturated zones in sandstone reservoirs of the Miocene Age. The rock physics modeling relates the reservoir properties (porosity, lithology, clay content) to elastic properties. Fluid substitution is done using Gassmann equations to calculate the elastic properties of the reservoir with CO_2 at different saturations using different fluid mixing theories. AVA analysis is done assuming a two-layer model, where the shale is used as a cap-rock with an underlying sandstone. The properties of the underlying sandstone (Vp, Vs, and density) were varied according to the fluid substitution modeling. The angle-dependent reflectivity depends on both the elastic properties of the sandstone and the properties of the overlying shale. The objective of the statistical classification is to discriminate pore fluid based on elastic properties. In this case, Vp/Vs and P-Impedance are the elastic properties that have the higher success rate discriminating between brine and CO_2.

The well log data from OCS 511 was used for this study. The well is located in the High Island Area (Figure 4.1). The following data were available for an interval of interest: P-wave velocity and S-wave velocity from sonic (Vp and VS), density (rho), volume concentration of shale (Vsh), water saturation (Sw), and effective porosity (phi). The well logs cover the intended reservoir sands from the Lower Miocene 2 (LM2) and the overlying shale (*Amph*.B) above the reservoir (Figure 4.2). Figure 4.3 shows the Vp-porosity crossplot for the Lower Miocene 2 (LM2) sandstones, colored coded by depth. The upper and lower Hashin-Strickman bound are also plotted represented by the blue and red lines, respectively. As can be seen the average porosity of the sandstone is close to 30%, and the sandstone data points are close to the lower Hashin-Strickman bound.

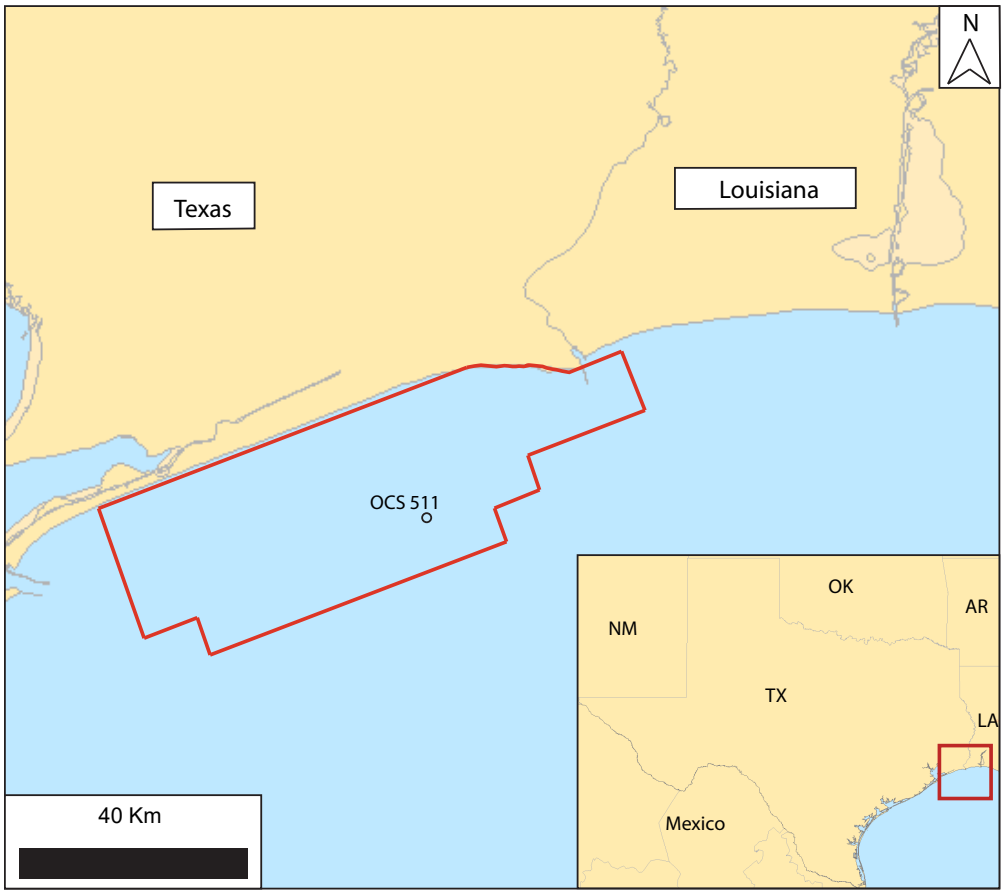

Figure 4.1: Location of the well OCS 511 in the area of study.

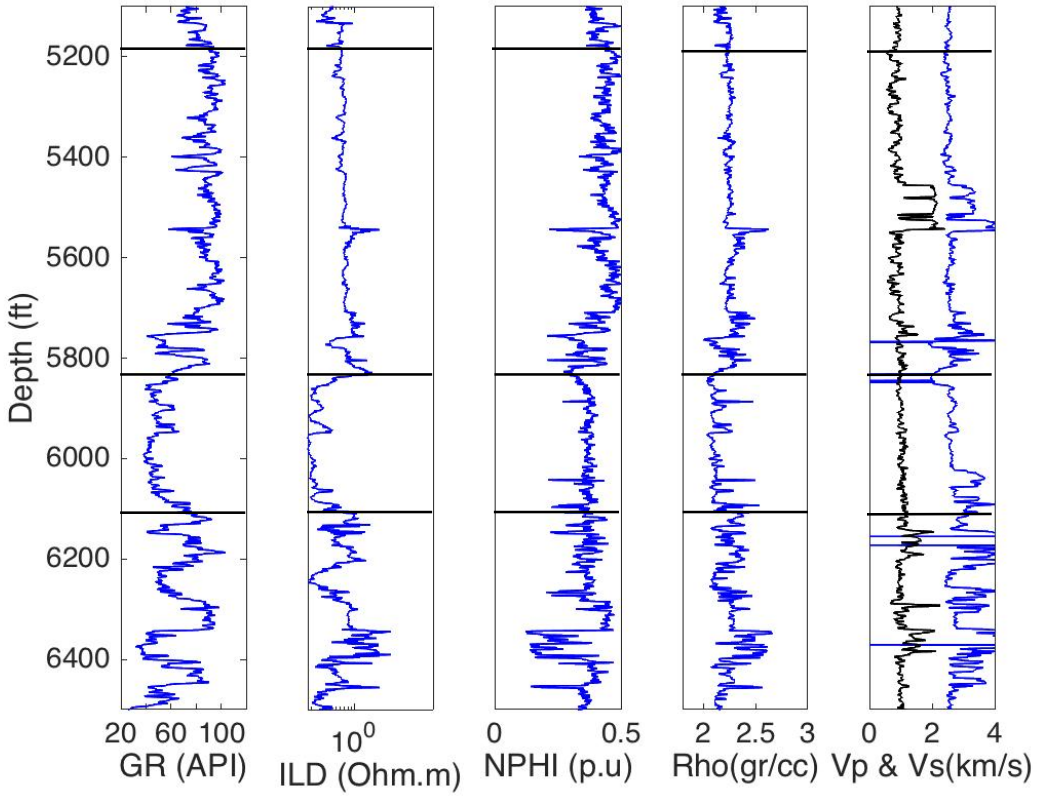

Figure 4.2: Gamma ray, deep resistivity, neutron porosity, compressional and shear velocity logs of the OCS 511 well. The black lines the top of the overlying shale (*Amph*. B) and the top and base of the Lower Miocene sandstone layer used in this study.

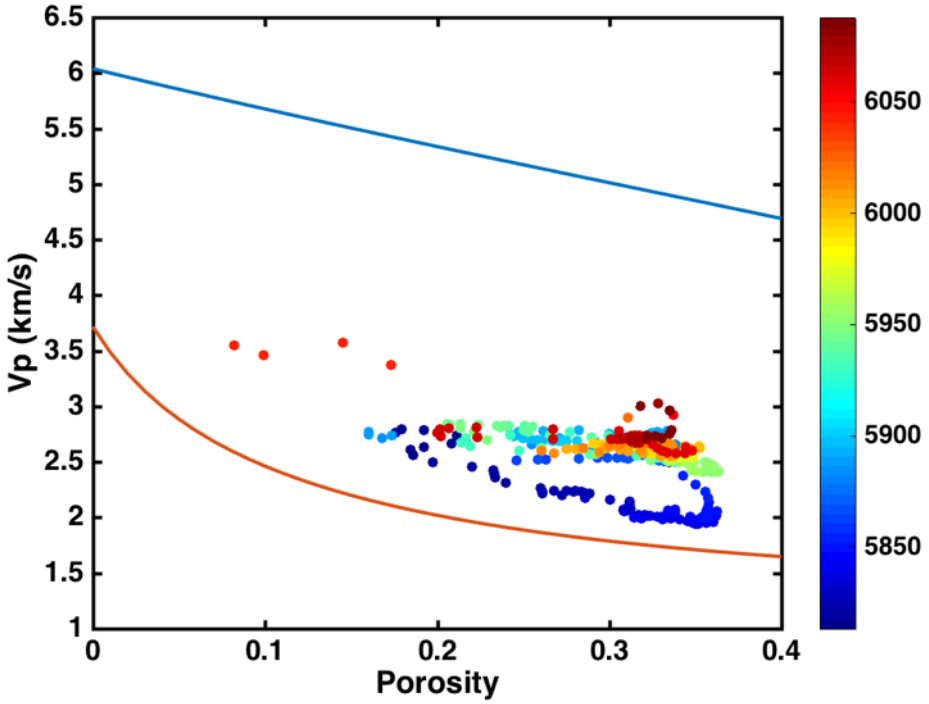

Figure 4.3: Porosity-velocity plot for the Lower Miocene sands. The blue and orange lines indicate the Hashin-Shtrikman upper and lower bound, respectively. The color bar indicates the depth of each point.

4.2 METHODOLOGY

4.2.1 Rock Physics Modeling

Previous work done on well log data from the inner continental shelf of the Texas Gulf of Mexico used showed that the soft sand model (Dvorkin and Nur, 1996) accurately matched well the data from the Lower Miocene 2 (LM2) section (Chapter 3; section 3.2.1). In Chapter 3 a single composition of clay and quartz was used for the soft sand model to represent Lower Miocene section in the rock physics modeling. That assumption was selected for simplicity. However, in this chapter because the analysis will focus on the

upper sand layer seen in well OCS 511 (Figure 4.1) the rock physics modeling is applied in more detail; selecting a more specific mineral composition of the sand. According to Dutton et al (2012) the Lower Miocene sandstones in the Upper Texas area of the Gulf of Mexico is dominantly composed of quartz, feldspar and the main reason for the loss of porosity is burial compaction. Table 4.1 shows the properties of the mineral and fluid used in the rock physics modeling. A description of the soft sand model can be found in Chapter 3.

Fluid / Mineral	Bulk Modulus (GPa)	Shear Modulus (GPa)	Density (g/cc)
Quartz	37	44	2.65
Feldspar	75.6	25.6	2.63
Clay	25	9	2.55
Brine	2.73	0	1.033
CO_2	0.0871	0	0.691

Table 4.1: Fluid and mineral properties used in rock physics modeling and fluid substitution analysis. The elastic properties of the fluids are obtained using the Batzle-Wang equation. The elastic properties of the minerals used are from Mavko et al. (2009).

4.2.2 Fluid Substitution

Fluid substitution calculations are a valuable tool for modeling various fluid scenarios. They are used to understand and predict how the saturation of different fluids in the pore space affect may affect the elastic properties of the rock. If the initial elastic properties of the sequestering formation (P and S-wave velocities, bulk density, porosity,

bulk modulus of the mineral) and the pore fluid properties (bulk modulus and density) at reservoir conditions, as well as the fluid saturation, Gassmann (1951) theory predicts the resulting effective bulk modulus, K_{sat} of the saturated rock using the following equations:

$$\frac{K_{sat}}{K_0 - K_{sat}} = \frac{K_{dry}}{K_0 - K_{dry}} + \frac{K_{fl}}{\phi(K_0 - K_{fl})}, \tag{4.1}$$

$$\mu_{sat} = \mu_{dry}, \tag{4.2}$$

where K_{dry} is the effective bulk modulus of the dry rock, K_{sat} is the bulk modulus of the rock with pore fluid, K_0 is the bulk modulus of the mineral of the rock, K_{fl} is the effective bulk modulus of the pore fluid, and ϕ is the porosity of the rock, μ_{sat} is the shear modulus of the rock with pore fluid, μ_{dry} is the shear modulus of the dry rock. The application of Gassmann's equation is based on the assumptions that the rock is isotropic with a homogenous mineral modulus, and pore pressure is equilibrated in the pore space (Gassmann, 1951).

To calculate K_{sat} of a rock saturated with a particular fluid, first we need to calculate the dry-bulk modulus of the rock K_{dry} using eq. 4.3. Then we calculate the bulk modulus of the rock saturated using eq. 4.4.

$$K_{dry} = \frac{K_{sat}(\phi\, K_0/K_{fl} + 1 - \phi) - K_0}{(\phi/K_{dry})\,(1/K_0 - 1/K_{fl}) + (1/K_0)(1/K_0 - 1/K_{dry})} \tag{4.3}$$

$$K_{sat} = \frac{\phi(1/K_0 - 1/K_{fl}) + 1/K_0 - 1/K_{dry}}{(\phi/K_{dry})\,(1/K_0 - 1/K_{fl}) + (1/K_0)(1/K_0 - 1/K_{dry})}. \tag{4.4}$$

The effective bulk modulus of the mineral matrix is calculated with the Voigt – Reuss – Hill average that is the average between the Voigt upper bound and the Reuss Lower bound (Mavko et al., 2009). The moduli for the minerals used is shown in Table 4.1. The effective modulus of a mixture of fluids can be calculated using the Voigt upper bound or the Reuss lower bound (Figure 4.4). The Voigt upper bound represents a patchy saturation and it is an arithmetic average of the moduli of the two fluids, while the Reuss is the harmonic average of the fluid moduli lower bound and represents homogenous saturation. The Voigt bound represents the stiffer way of mixing two fluids. On the other hand, the Reuss bound represents the softest way of mixing two fluids.

The properties of the CO_2 change drastically with temperature and pressure. To calculate the elastic properties of the CO_2 at reservoir conditions the Batzle-Wang equations are used. Table 4.2 shows the bulk modulus for the mixture of brine and CO_2 at different parentages at a temperature of 56 degrees Celsius and pore pressure of 18MPa. These percentages include 0, 20, 40, 60, 80, and 100% CO_2 saturation, with brine composing the complementary percent.

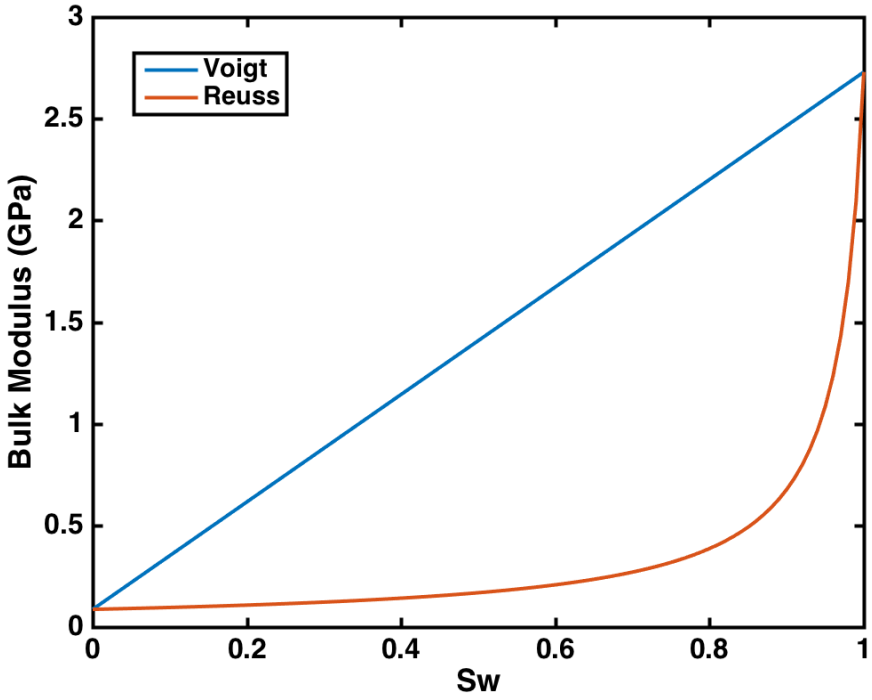

Figure 4.4: Bulk modulus of variable mixture between CO_2 and brine, with different water saturations (Sw). The blue line represents the Voigt bound (arithmetic average) and the red line represents the Reuss bound (harmonic average).

Bound \ Bulk Modulus (GPa)	20% CO_2	40% CO_2	60% CO_2	80% CO_2	100% CO_2
Voigt	2.2070	1.6729	1.1443	0.6157	0.0871
Reuss	0.3863	0.2079	0.1422	0.1081	0.0871

Table 4.2: Bulk Modulus and density for different percentages of CO_2 and Brine used in fluid substitution

4.2.3 AVA Modeling

Amplitude variation with angle (AVA) analysis of seismic reflections exploit changes of seismic amplitude as a function of the angle of incidence in order to detect changes in reservoir properties. The Zoeppritz (1919) equations, shown below, describe how the reflection coefficient changes as a function of the angle of incidence for a two-layer model.

$$\begin{pmatrix} \sin(\theta_1) & \cos(\phi_1) & -\sin(\theta_2) & \cos(\phi_2) \\ -\cos(\theta_1) & \sin(\phi_1) & -\cos(\theta_2) & -\sin(\phi_2) \\ \sin(2\theta_1) & \frac{V_{P1}}{V_{S1}}\cos(2\phi_1) & \frac{\rho_2 V_{S2}^2 V_{P1}}{\rho_1 V_{S1}^2 V_{P2}}\sin(2\theta_2) & -\frac{\rho_2 V_{S2} V_{P1}}{\rho_1 V_{S1}^2}\cos(2\phi_2) \\ -\cos(2\phi_1) & -\frac{V_{S1}}{V_{P1}}\sin(2\phi_1) & -\frac{\rho_2 V_{P2}}{\rho_1 V_{P1}}\cos(2\phi_2) & -\frac{\rho_2 V_{S2}}{\rho_1 V_{P1}}\cos(2\phi_2) \end{pmatrix} \begin{pmatrix} R_{PP} \\ R_{PS} \\ T_{PP} \\ T_{PS} \end{pmatrix} = \begin{pmatrix} -\sin(\theta_1) \\ -\cos(\theta_1) \\ \sin(2\theta_1) \\ -\cos(2\phi_1) \end{pmatrix}$$

To do the AVA modeling each layer needs a value of p-wave and s-wave velocity, and density. For this study, the values used were taken from well logs (sonic and density logs). When using a single value of Vp, Vs and density for each layer, the AVA modeling result is a single curve of PP reflectivity for the shale-sandstone interface. This single curve does not account for the intrinsic geologic variability of each layer and the interface between the two layers. To account for the possible lateral variability of each layer Monte Carlo simulation is used to assess uncertainties in seismic signature related to the natural variability within each layer. It is important to make sure that the Monte Carlo simulation preserves the distributions and the Vp-Vs and Vp-density correlations of the original data (Avseth, 2005). The histograms of the elastic properties computed with the log data were compared with the equivalent histograms calculated with the Monte Carlo data values.

Figure 4.5 reveals that initial Vp, Vs, and density distributions for the overlying shale are preserved after Monte Carlo simulations.

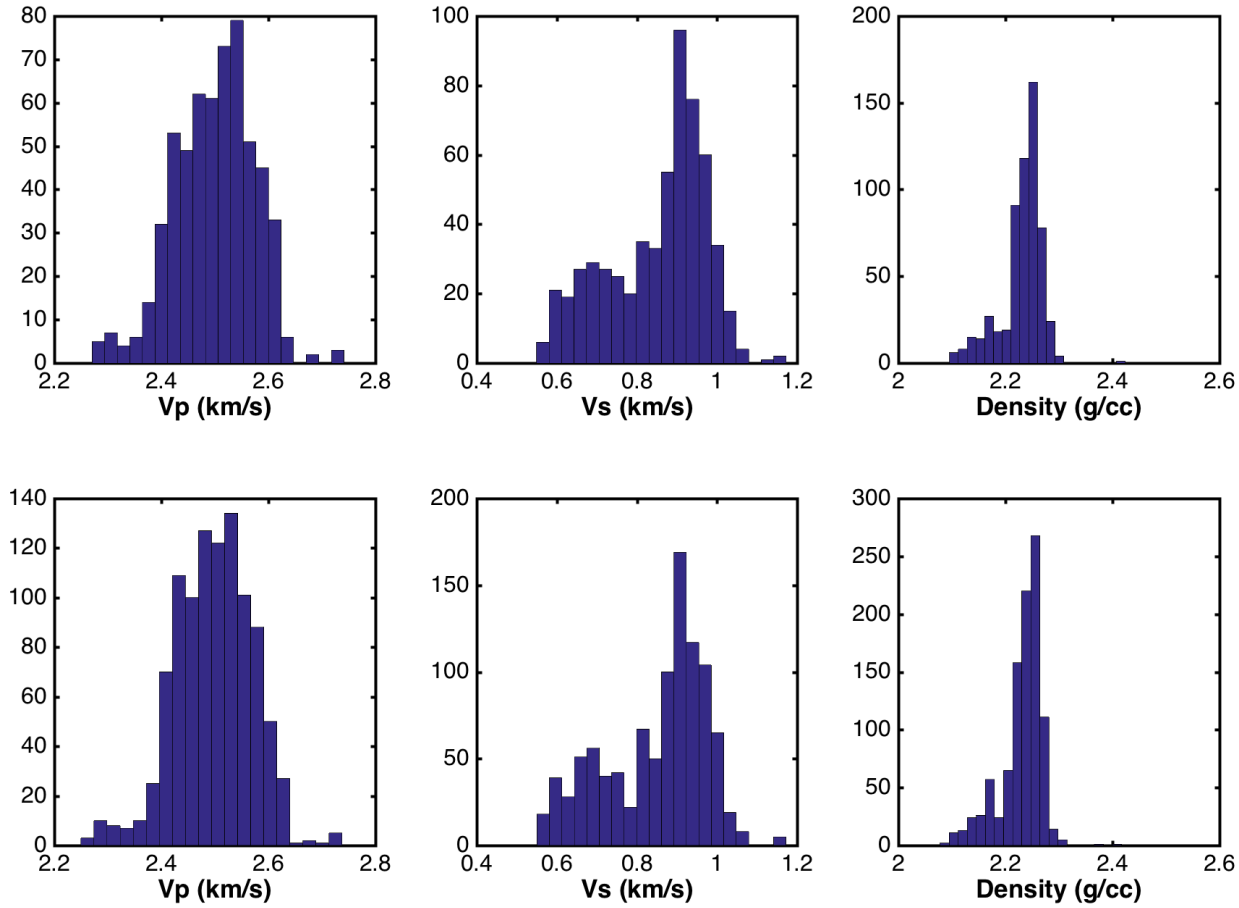

Figure 4.5: Histograms of Vp, Vs, and density from well log data (top) and Monte Carlo Simulation (Bottom) for the overlying shale.

Five hundred reflectivity simulations were calculated from the Monte Carlo simulated properties for the overlying shale and the reservoir sandstone for each different fluid composition (0, 20, 40, 60, 80, and 100% CO_2) for the two different fluid mixing

methods (Voigt and Reuss). The reflectivity simulation was calculated using Zoeppritz equation with angle of incidence from 0 to 30 degrees.

4.2.4 Classification

The goal is to evaluate if we can use seismic attributes, for example, P-impedance and Vp/Vs to discriminate and classify between different fluids (CO_2 and Brine) in the pore space. To do this, crossplots were constructed for Vp/Vs and P-impedance for the different classes (e.g., 0, 20, 40, 60, 80, and 100% CO_2), using the velocities and densities obtained from the fluid substitution (Figure 4.6). Then, the bivariate PDFs were computed for each class and using the Mahalanobis distance to data was classified. Using the derived PDFs of seismic attributes, feasibility evaluations are made about which set of seismic attributes contains the most information for the problem (Bosch, 2010). Figure 4.7 illustrates the concept of classification where we have two classes and two elastic properties, z1 and z2, representing for example Vp/Vs and P-impedance. The bivariate PDFs for each class are represented in green and orange contours. The classification is applied point-by-point, where each point is classified to a certain class according to the minimum Mahalanobis distance to each cluster (Duda and Hart, 1973; Fukunaga, 1990).

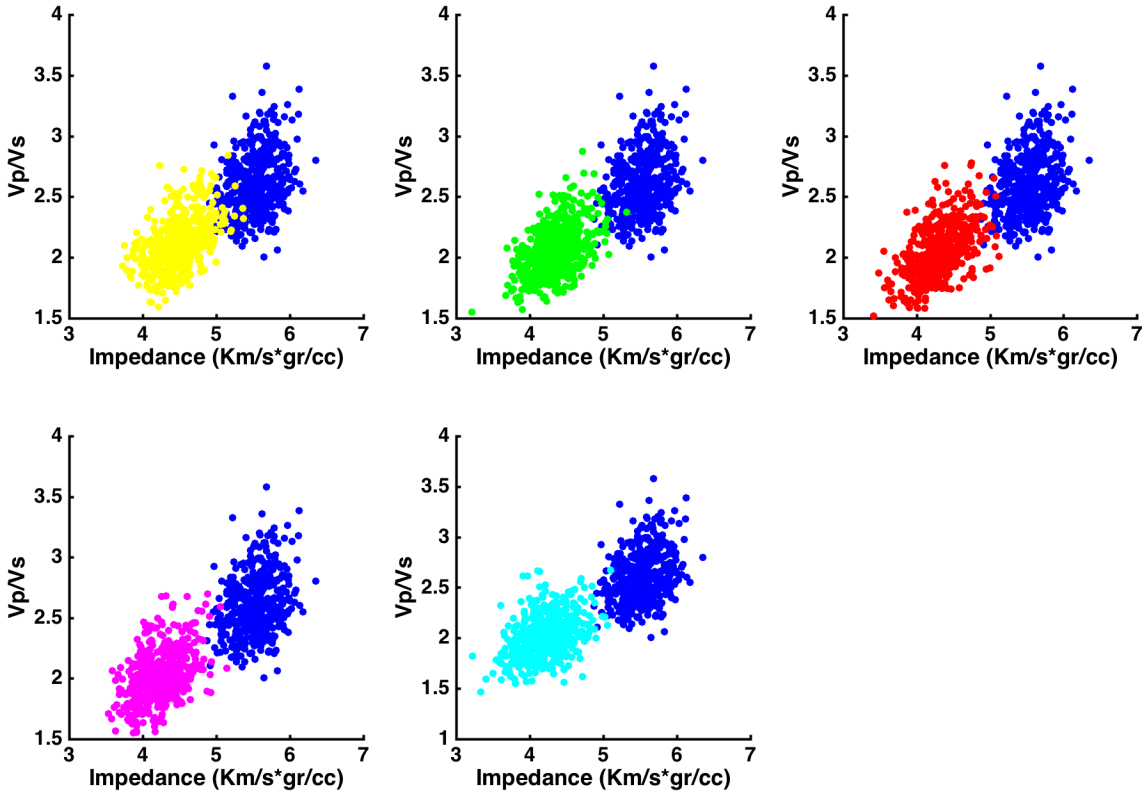

Figure 4.6: Crosplots of Vp/Vs versus P-Impedance for the different classes (20%, 40%, 60%, 80%, and 100% CO_2) calculated with the Reuss bound and the brine saturated sand. The blue points represent the 0% CO_2, yellow 20%, green 40%, red 60%, magenta 80%, and cyan 100% CO_2.

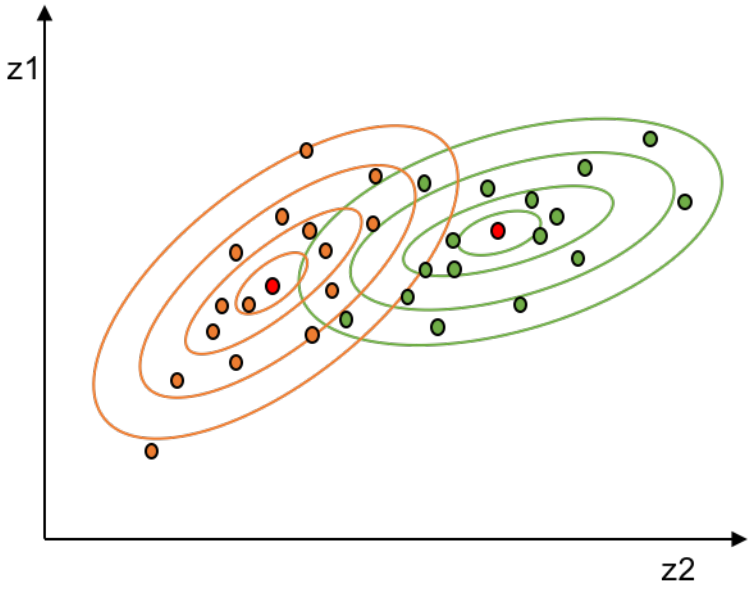

Figure 4.7: Crossplot of properties z1 and z1 for two classes to illustrates the concept of classification. The orange and green contours represent the bivariate pdfs for each class. The classification scheme is applied to each point, and it is classified to a certain class according to the minimum Mahalanobis distance each to each cluster(orange or green).

The Mahalanobis distance is defined as:

$$M^2 = (x - \mu_i)^T \sum^{-1} (x - \mu_i)\,, \tag{4.5}$$

where x is the sample feature vector (measured attribute), μ_i are the vectors of the attribute means for the different classed, and Σ is the covariance matrix of the training data.

The uncertainty in predicting the pore fluid from elastic properties will be directly linked to the degree of overlap between the ranges of values (Doyen, 2007), and because of the overlap among the different classes the classification will not be perfect. To compute the classification success, the elements of the classification confusion matrix are estimated.

The diagonal elements of the matrix are the success rate for each class, while the off-diagonal elements are probabilities of misclassification (Avseth, 2005). The parameter that shows the highest success to discriminate between brine and CO_2 was Vp/Vs as a function of P-Impedance. Each fluid composition was compared against each other for both patchy saturation and homogeneous saturation.

4.3 RESULTS

4.3.1 Rock physics Modeling

The results from the rock physics modeling can be seen in Figure 4.8. The blue, green, red and black are modeled using the uncemented sand model varying the concentration of the different mineral components of the rock and fluid. The blue, green, and red curves are the sands saturated with brine, and the black curve was modeled with a 70% gas saturation. Table 4.1 shows the values of the moduli used for the minerals and fluids.

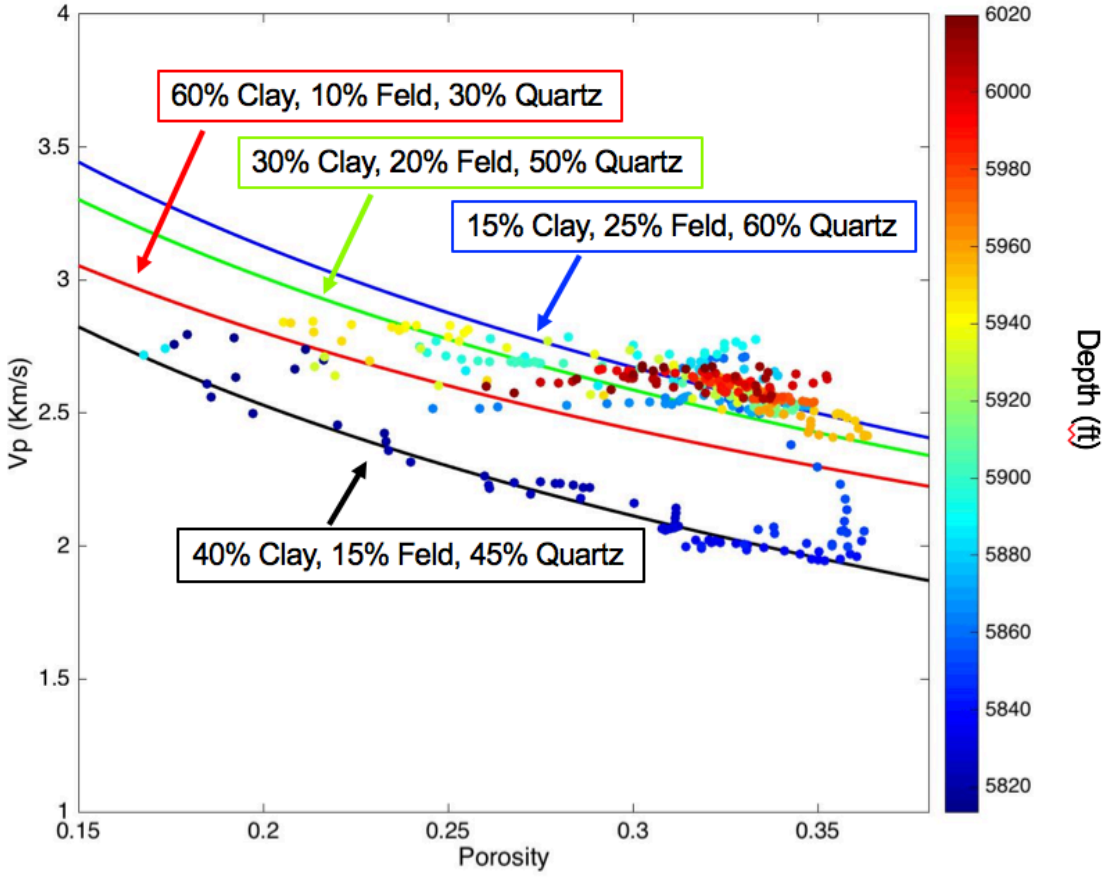

Figure 4.8: Vp versus porosity from the Lower Miocene sandstone. The color represents the depth of each point. The blue, green, red, and black lines represent the uncemented sand model with different components increasing the clay content. The in situ fluid model in the blue, green, and red curve are water, whereas the in situ fluid used in the black curve is gas.

The rock physics modeling is useful to establish relationships between reservoir properties and seismic properties. Using rock physics models, the effect of clay content on the p-wave velocity and porosity can be identified, and it helps to correlate the mineral composition of the rock and the mineral moduli that are needed for the fluid substitution.

4.3.2 Fluid Substitution

Figure 4.9 shows the velocities obtained from fluid substitution using Gassmann equations with different fluid in the pore space. The red, yellow, purple, green, cyan, and magenta lines show the velocities modeled with 0, 20, 40, 60, 80, and 100% CO_2 saturation, respectively. The blue line represents the measured velocity from the well logs. The upper part of the sandstone is saturated with gas, and the curve overlaps with the modeled velocities for 100% CO_2 saturation, from 5867 ft the in-situ fluid is water, and the curve overlaps with the 100% brine curve. The left panel in Figure 4.9 shows the p-wave velocity modeled using the Voigt upper bound for the bulk modulus for the different fluid compositions. The Voigt bound represents the patchy saturation model. The middle panel in Figure 4.9 shows the p-wave velocity using the Reuss lower bound for the fluid moduli. The Reuss average implies that just a few percent of CO_2 injected in the pores can significantly lower the P-wave velocity of the sequestering formation. The right panel in Figure 4.9 shows the s-wave velocity. The slight change in the velocity is due to the change in bulk density for the different saturations of CO_2.

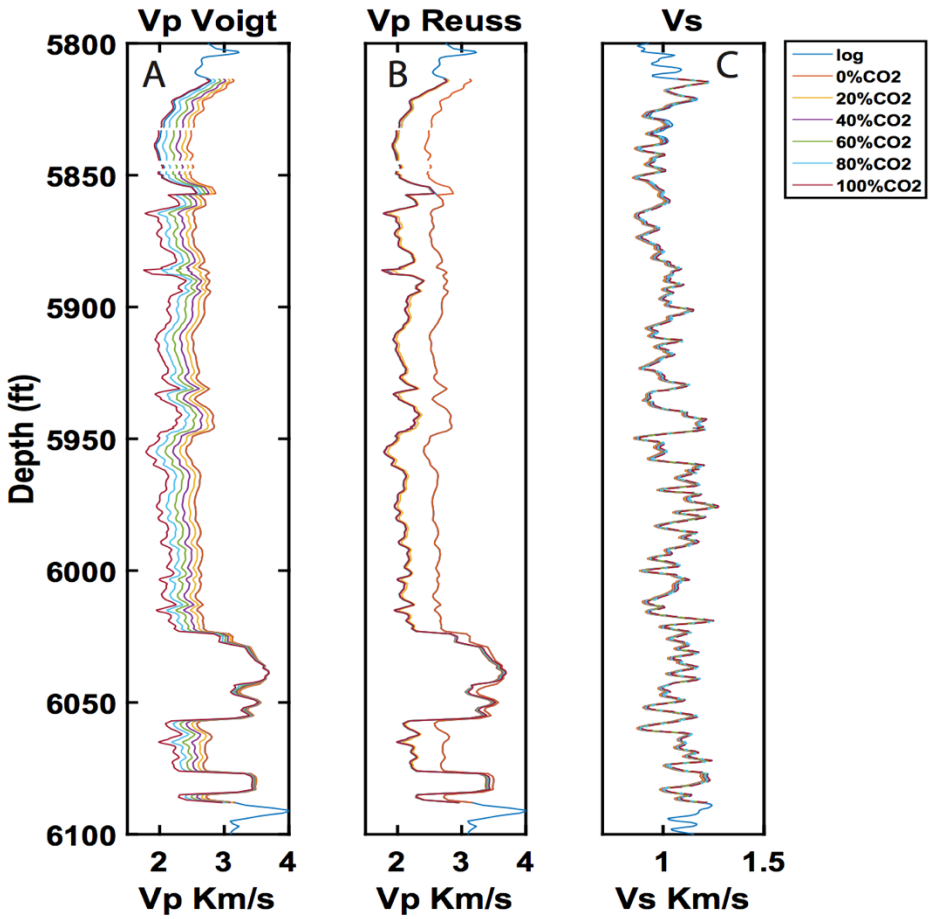

Figure 4.9: A) Shows p-wave velocities for the LM2 sandstone with different saturation of CO_2, where the bulk fluid modulus is calculated from the Voigt average B) shows the same as in A, but the fluid moduli were calculated with the Reuss average. C) Shows the s-wave velocity. The red, yellow, purple green, cyan and magenta curves represent the 0, 20, 40, 60, 80, 100% CO_2, respectively. The panel A shows a constant spacing because the Voigt average is linear. Panel B shows a big separation between the curves with 100% brine and CO_2, indicating that a low concentration of CO_2 changes the moduli significantly.

The bulk moduli of the fluid have an important role in the velocity results obtained from the fluid substitution. When considering the Reuss average to determine the bulk modulus of the fluid mixture, the p-wave velocity of the rocks significantly drops with CO_2

saturations of 20%. For saturations between 20% and 100% the velocity decreases a small percent. When the bulk modulus of the fluid is calculated using the Voigt bound (the patchy case), the velocities decreases in a linear trend when the CO_2 saturation increases.

4.3.3 AVA MODELING

Figures 4.10 and 4.11 show the reflection coefficients calculated using the Zoeppritz equations for angles between 0 and 30 degrees. Five hundred simulations were computed for different saturations of CO_2. Figure 4.10 shows the angle-dependent reflectivity using the Voigt bound. The black line in each case represents the mean curve for each case. Figure 4.11 shows the reflectivity using the Reuss bound.

In Figure 4.10 and 4.11 the mean curve for 0% CO_2 shows a reflectivity close to 0. This indicates that the contrast in impedance between the overlying shale and the sandstone fully saturated with brine is barely noticeable, but when the saturation of CO_2 in the pore space increases the contrast in impedance, generating a more negative reflection. One important aspect shown in Figure 4.11 is that a small concentration of CO_2 in the pore space creates a considerable change in PP reflectivity, when the fluid is mixed using the Reuss bound. This makes it difficult to differentiate changes in the reflection coefficient when the CO_2 saturation increases above 20%.

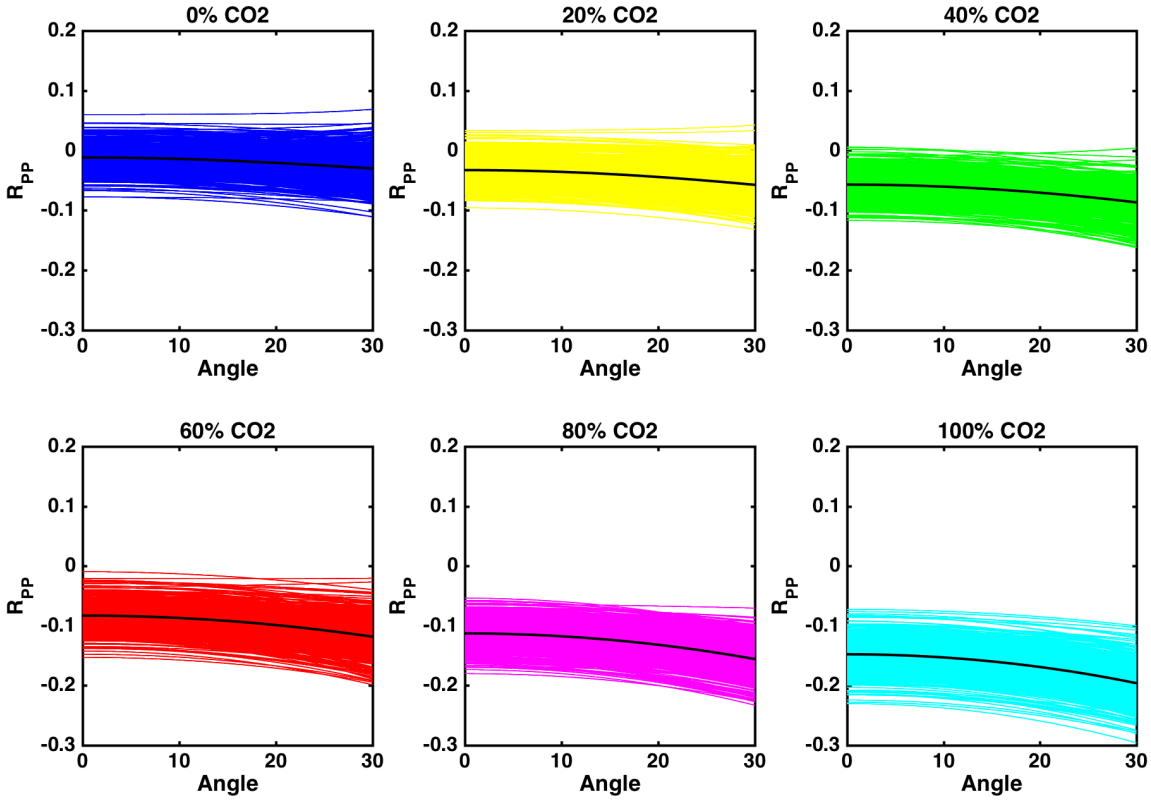

Figure 4.10: Angle dependent reflectivity for the overlying shale and the Lower Miocene 2 (LM2) sandstone. The x axes are the reflection coefficient and the y axes are the incident angle from 0 to 30 degrees. The black line in each panel represent the average reflectivity for each class. The blue line is the for 0% CO_2, yellow 20% CO_2, green 40% CO_2, red 60% CO_2, magenta 80% CO_2 and cyan 100% CO_2 for patchy saturation

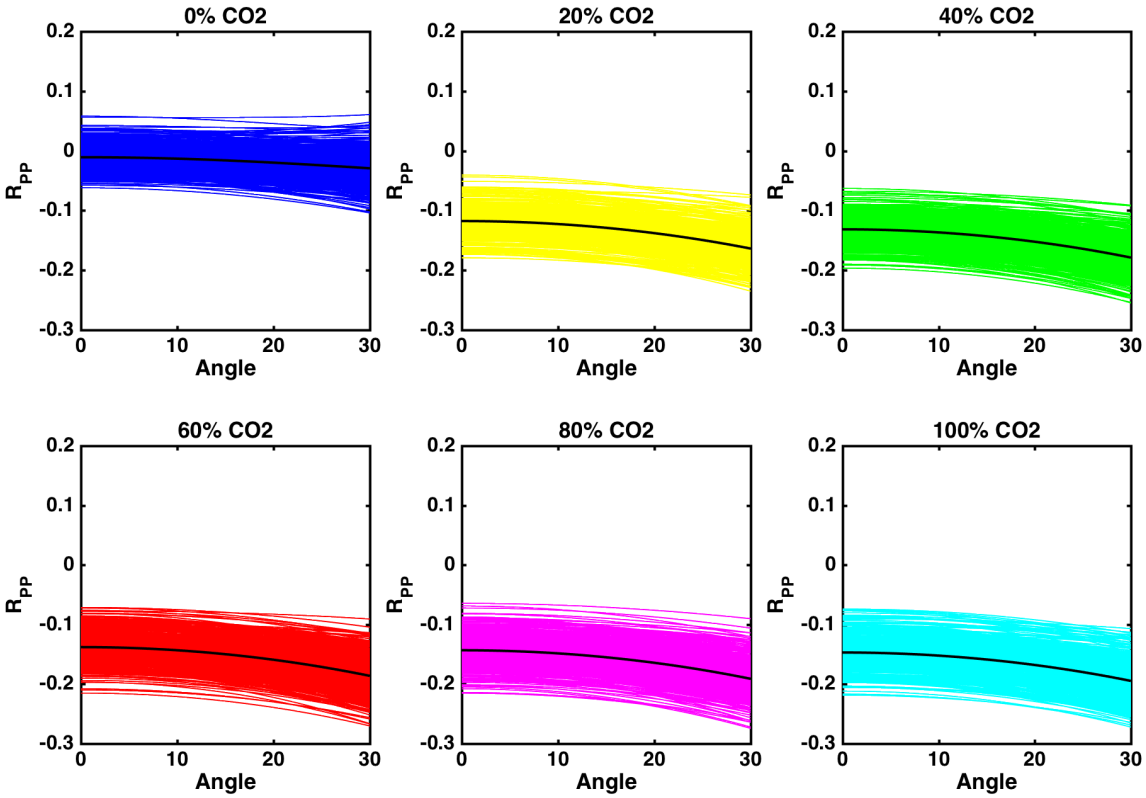

Figure 4.11. Angle dependent reflectivity for the overlying Amph.B shale and the LM2 sandstone. The x axes are the reflection coefficient and the y axes are the incidence angle from 0 to 30 degrees. The black line in each panel represent the average reflectivity for each class. The blue line is the for 0% CO_2, yellow 20% CO_2, green 40% CO_2, red 60% CO_2, magenta 80% CO_2 and cyan 100% CO_2 for homogenous saturation. The reflectivity is highly affected by low concentration of CO_2, which makes it difficult to see differences in the reflection coefficient when the CO_2 saturation increases above 20%.

The variation in the AVA responses due to fluid composition is evident. This variation in the AVA response can be explain by the soft frame of the rock. The soft frame of the rock increases the sensitivity of the rock to the elastic properties if the fluid in the pore space. The Lower Miocene sandstones are rocks with high porosity, at relative shallow depth and low pressure. Under these conditions significant variation in the PP reflectivity is expected when the pore fluid changes.

4.3.4 CLASSIFICATION

Vp/Vs as function of P-impedance is the combination of properties that resulted in the highest classification success. Tables 4.3 and 4.4 show the classification confusion matrix for each facies for the two different fluid mixture theories. Figures 4.12 and 4.13 show the bivariate PDFs for the 0% CO_2 and the other different classes (20%, 40%, 60%, 80%, and 100%) for the patchy model and the uniform saturation. The blue contours in each figure represent the 0% CO_2, the yellow, green, red, magenta, and cyan represent 20%, 40%, 60%, 80%, and 100% CO_2.

Figure 4.12 shows the plot of Vp/Vs – P-impedance bivariate PDFs for the patchy saturation model comparing the 0% CO_2 saturation (blue contours) with different saturations of CO_2 (20%, 40%, 60%, 80%, and 100%). The 0% CO_2 and 20% CO_2 PDFs overlap significantly but when the CO_2 saturation increases the overlap between the PDFs decreases. Table 4.3 shows the classification confusion matrix for the patchy saturation model, the elements of the principal diagonal of the matrix are the classification success of each class. For saturations between 40% and 80% CO_2 the classification success is low. For 40% CO_2 saturation the success rate is 0.39, which mean that only 39% of the data is being classified correctly, 25% is being classified incorrectly as 20% CO_2, and 23% of the data is being classified as 60% CO_2. In the case 80% CO_2 saturation the success rate is 0.384, and 22% of the data is wrongly classified as 60% CO_2 and 31% of the data is incorrectly classified as 100% CO_2.

In the case of the homogenous saturation model Figure 4.13 shows a good separation between the 0% CO_2 (blue contours) and the different classes. When the PDFs of the 20%, 40%, 60%, 80%, and 100% CO_2 are compared to each other in Figure 4.14 they overlap significantly. The elements of the principal diagonal of the confusion matrix

for the homogenous saturation model shown in Table 4.4 show low classification success for CO_2 saturation between 20% and 100%.

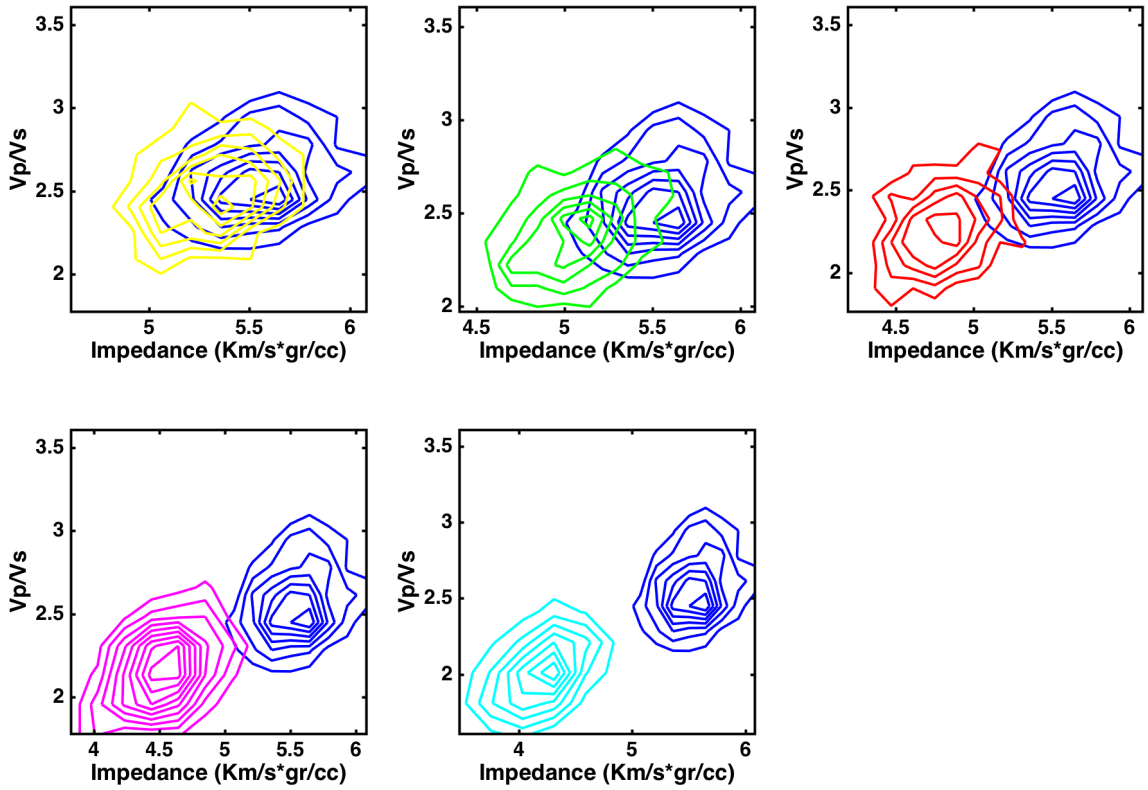

Figure 4.12: Bivariate PDFs for the 0% CO_2 and the other different classes (20%, 40%, 60%, 80%, and 100%) for patchy saturation. The blue contours in each figure represent the 0% CO_2, the yellow, green, red, magenta, and cyan represent 20%, 40%, 60%, 80%, and 100% CO_2.

True\Predicted	0% CO_2	20% CO_2	40% CO_2	60% CO_2	80% CO_2	100% CO_2
0% CO_2	0.840	0.068	0.056	0.036	0	0
20% CO_2	0.072	0.692	0.200	0.036	0	0
40% CO_2	0.078	0.250	0.390	0.234	0.048	0
60% CO_2	0.040	0.010	0.196	0.520	0.210	0.024
80% CO_2	0.004	0.004	0.070	0.224	0.384	0.314
100% CO_2	0	0	0.008	0.056	0.206	0.730

Table 4.3: Confusion classification matrix for minimum Mahalanobis distance. The fluid properties were calculated using the Voigt average. The diagonal shows the success rate for the classification of each class. Showing a good overall classification

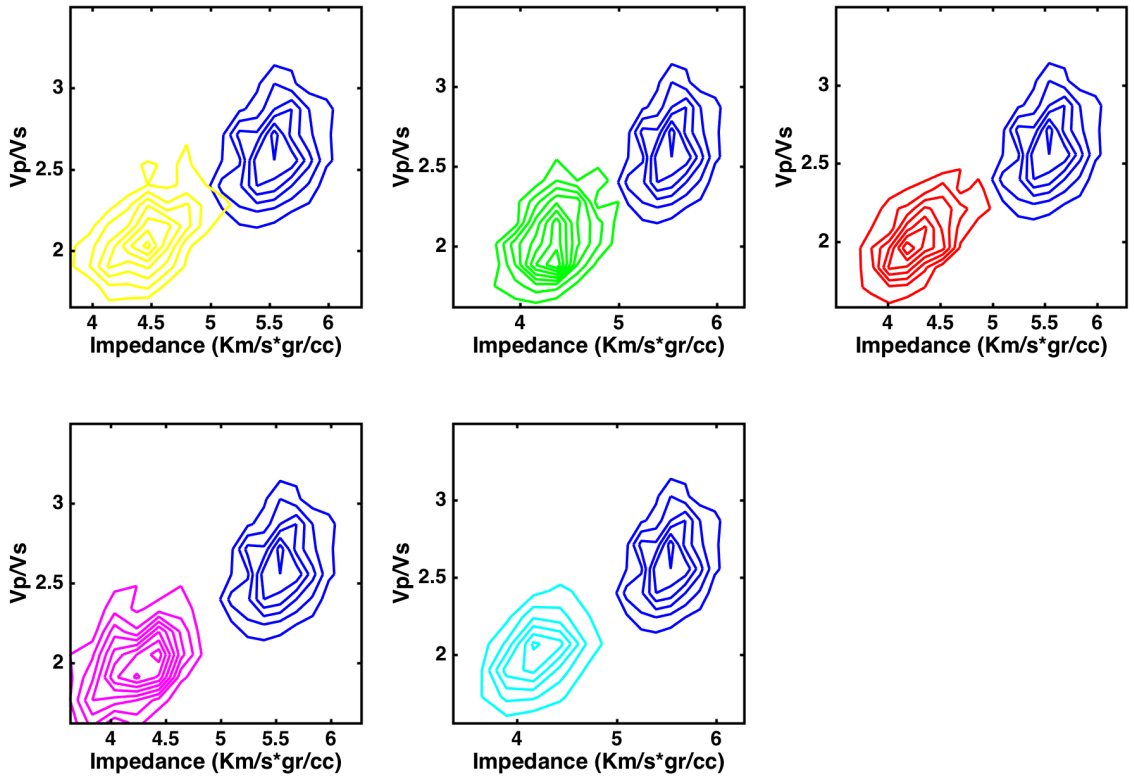

Figure 4.13: Bivariate PDFs for the 0% CO_2 and the other different classes (20%, 40%, 60%, 80%, and 100%) for uniform saturation. The blue contours in each figure represent the 0% CO_2, the yellow, green, red, magenta, and cyan represent 20%, 40%, 60%, 80%, and 100% CO_2.

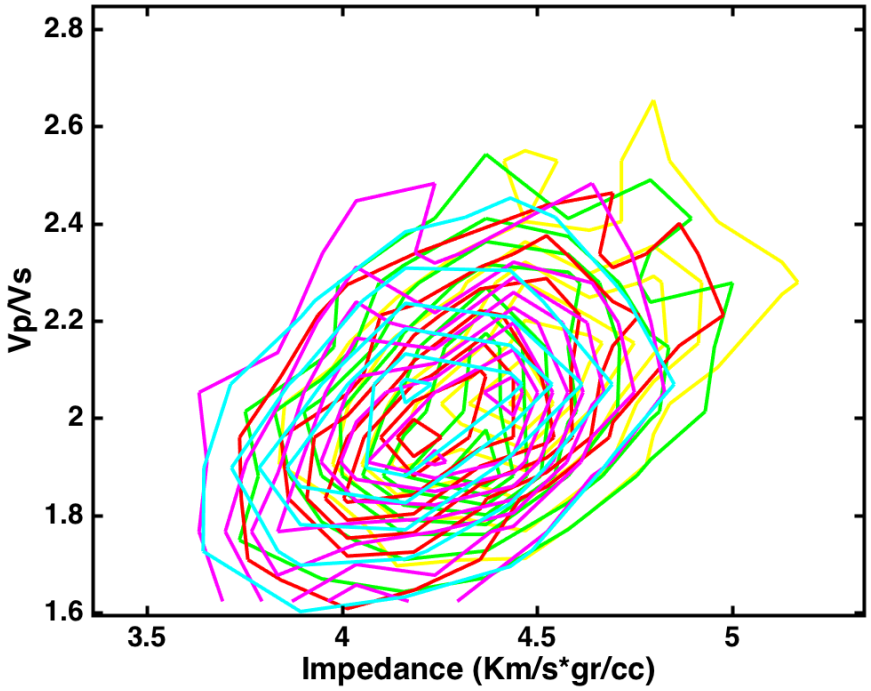

Figure 4.14: Bivariate PDFs for the classes (20%, 40%, 60%, 80%, and 100%) for uniform saturation. The yellow, green, red, magenta, and cyan contour represent 20%, 40%, 60%, 80%, and 100% CO_2, respectively. The overlap shows the uncertainty in discriminate between different CO_2 saturations, when the fluid properties were calculated using the Reuss average (uniform saturation)

True\Predicted	0% CO_2	20% CO_2	40% CO_2	60% CO_2	80% CO_2	100% CO_2
0% CO_2	0.976	0.024	0	0	0	0
20% CO_2	0.026	0.554	0.106	0.104	0.104	0.106
40% CO_2	0.006	0.370	0.104	0.164	0.132	0.224
60% CO_2	0.006	0.328	0.094	0.122	0.142	0.308
80% CO_2	0.004	0.288	0.094	0.112	0.138	0.364
100% CO_2	0.0120	0.230	0.094	0.134	0.158	0.372

Table 4.4: Confusion classification matrix for minimum Mahalanobis distance. The fluid properties were calculated using the Reuss average. The diagonal shows the success rate for the classification of each class.

The overall results from the classification show that using Vp/Vs and P-Impedance could be possible to distinguish between brine and CO_2, but obtaining the CO_2 saturation from these properties will be difficult. When comparing the results from the two mixing fluid theories, the uncertainty using the homogenous saturation model is much higher than using the patchy saturation model. This uncertainty is due to the overlapping of the PDFs, (Figure 4.14) making difficult to distinguish between CO_2 saturations.

4.4 CONCLUSION

This study showed the sensitivity of the elastic properties of the sandstone reservoirs of the Lower Miocene 2 stratigraphic interval to changes in variable CO_2 saturations. Using well log data, the AVA modeling and the classification using Vp/Vs and P-Impedance showed good results. The AVA modeling is reliable when examining the fluid substitution in the LM2 sandstone reservoirs. The soft frame of the rock makes the rock sensitive to the increases in CO_2 saturation when compared to brine. This indicates

the likely ability of the seismic methods to monitor injection and movement of CO_2 in this rock in the future.

The type of saturation of the CO_2 after injection has a great impact on the ability of the seismic methods to differentiate the amount of CO_2 in the pore space. In the case of homogenous saturation, it will be extremely difficult to differentiate between 20% of CO_2 or 80% CO_2. This is because the compressibility of the fluid for homogenous CO_2 saturations higher than 20% is small. This creates small changes in the elastic properties of the rock that will not be easy to observe with seismic data.

The mineral composition of the rock will hardly affect its sensitivity to CO_2. The increase or decrease of feldspar or clay will not cause a significant change in the bulk modulus of the dry rock. The depth and pressure will play a more important role in the sensitivity to CO_2 of Lower Miocene sands in other parts of the northern Gulf of Mexico. The increase of effective pressure will make the frame of the rock stiffer reducing its sensitivity to changes in CO_2 volumes.

Chapter 5: Conclusions and Future Work

5.1 CONCLUSIONS

This study quantitatively evaluates the CO_2 storage capability of the Lower Miocene brine-filled sandstones in the inner continental shelf of the Texas Gulf of Mexico using 3D seismic and well log data. This study has demonstrated the application of quantitative methods to: (1) estimate reservoir properties to characterize intended CO_2 reservoirs, and (2) understand the effect of injected CO_2 on the elastic properties of the Lower Miocene sandstones.

In Chapter 3, the quantitative method applied successfully estimated the reservoir properties that has the greater impact in the characterization of intended CO_2 reservoirs. The rock physics modeling described the relationship between elastic properties and porosity and mineralogy using the soft sand model. From the simultaneous seismic inversion P-impedance, S-impedance, and density volumes were obtained. Then using rock physics transforms on the seismically derived elastic properties, the porosity and lithology were estimated. The main intention of this work was to determine the effectiveness of workflows and methodologies that have been successfully applied in the oil and gas industry for characterizing reservoirs for CO_2 storage. Although not undertaken as part of the thesis research, these results could be the used for storage capacity estimation and CO_2 migration simulation.

Chapter 4 studied the sensitivity of the Lower Miocene sandstones to changes in CO_2 saturation. The AVA response showed that the seismic response is sensitive to the pore fluid. The noticeable changes in the seismic amplitude when the CO_2 replaces brine in the pores space is due to the soft frame and high porosity of the sandstones. Statistical classification showed that a combination of P-impedance and Vp/Vs is the best way to successfully differentiate between brine and injected CO_2. The high sensitivity to CO_2 of

the seismic response in the Lower Miocene section makes the applicability of seismic methods likely to be successful in monitoring future injected CO_2.

The main contribution of this work is providing a workflow that could be used in the inner continental shelf of the Gulf of Mexico to better characterize reservoir properties and find the more appropriates zones to storage CO_2. The workflow used not only takes into the account the reservoir properties but also the impact of CO_2 in the elastic properties to successfully monitor the future injected CO_2. In general, the Lower Miocene section in the offshore areas of the Texas Gulf of Mexico show favorable properties for CO_2 storage. The high porosity of the sands implied a high capacity of CO_2 storage, and the high sensitivity to CO_2 saturation indicates future CO_2 injected is likely to be successfully monitored by using seismic methods.

5.2 FUTURE WORK

In this work a quantitative method was used to estimate reservoir properties. The workflow includes rock physics modeling and simultaneous seismic inversion. Accounting only for rock types and fluids sampled at the wells can lead to biased predictions of reservoir properties. Future work could be done integrating geological information into the workflow. Accounting for the geological model could improve the quantitative estimation of rock properties from inverted seismic data. Also the integration of petrophysical models into the workflow could help to estimate other reservoir properties. Using petrophysical models that relate porosity and clay content, could help improve the characterization of the intended CO_2 reservoirs, making possible the estimation of the clay content within reservoir.

Regarding the sensitivity analyses some assumptions were made in this study. One of them was that the pore pressure does not change before and after the injection of CO_2 for the AVA modeling. The change of pore pressure during the injection of CO_2 could affect the impedance of the reservoir. Taking into account these changes in pressure during the injection of CO_2 could help to improve the accuracy and the validity of the results. This work also assumed that the injected CO_2 replaces only brine. In the case of CO_2 replacing hydrocarbon or a combination of hydrocarbon and brine, the change in elastic properties might not be large enough to be detected using seismic methods. Further modeling should be done to account for different in situ fluids within the reservoir.

This study focused on the characterization of the Lower Miocene sandstone to study whether or not could be used as a reservoir for CO_2 storage. The results from this study could be used in additional analysis; the estimated porosity volume could be used to calculate the storage capacity of CO_2 of the Lower Miocene section and CO_2 migration simulation, which may be preferable to extrapolating these properties from wells into statistically generated volumes.

References

Aki, K., and P. G. Richards, 2002, Quantitative Seismology, 2nd Edition: W. H. Freeman and Company.

Arts, Rob; Chadwick, Andy; Eiken, Ola; Thibeau, Sylvain; Nooner, Scott. 2008 Ten years' experience of monitoring CO_2 injection in the Utsira Sand at Sleipner, offshore Norway. First Break, 26. 65-72.

Avseth, P., Mukerji, T., Mavko, G., 2005. Quantitative Seismic Interpretation. Cambridge University Press, New York.

Bachrach, R., 2006, Joint estimation of porosity and saturation using stochastic rock-physics modeling: Geophysics, **71**, no. 5, O53–O63, doi: 10.1190/ 1.2235991.

Backus, G.E., 1962, Long-wave elastic anisotropy produces by horizontal layering. Journal of Geophysical Research 68, 4427-4440.

Batzle, M., and Z. Wang,1992, Seismic properties of pore fluids: Geophysics, 57, No. 11, 1396-1408.

Biot, M.A., 1956. Theory of propagation if elastic waves in a fluid saturated porous solid. I. Low-frequency range. Journal of the Acoustical Sociaty of America 28, 168-178.

Carter, R. W., 2014, Fluid Characterization at the Cranfield CO_2 Injection Site: Quantitative Seismic Interpretation from Rock-Physics Modeling and Seismic Inversion. Phd. Dissertation. The University of Texas at Austin.

Carter, R. W., and Spikes, K. T., 2013, Sensitivity Analysis of Tuscaloosa Sandstone to CO_2 Saturation, Cranfield fieldm Cranfield, Ms: Intertacional Journa of Greenhouse Gas Control.

Chadwick, R. A., R. Arts, and O. Eiken, 2005, 4d Seismic Quantification of a Growing Co2 Plume at Sleipner, North Sea: Geological Society, London, Petroleum Geology Conference series, 6, 1385-99.

Dvorkin J., Gutierrez M., and Grana D., 2014, Seismic reflection of rock properties, Cambridge University Press.

Dvorkin, J. and Nur, A., 1996. Elasticity of high-porosity sandstone: theory for two North Sea datasets. Geophysics 61, 1363-1370.

Friedman, S. J., 2007, Geological Carbon Dioxide Sequestration: Elements, v. 3, p. 179-184.

Galloway, W. E., 1989, Depositional framework and hydrocarbon resources of the early Miocene (Fleming) episode, Northwest Gulf-Coast Basin: Marine Geology, v. 90, p. 19–29.

Galloway, W. E., 2008, Depositional evolution of the Gulf of Mexico sedimentary basin, in A. D. Miall, ed., The sedimentary basins of the United States and Canada: New York, Elsevier, v. 5, p. 505–549.

Gassmann, F., 1951. Uber die elastizitat poroser medien. Vierteljahrsschrift Natur-wissenschaften Gesellschaft 96, 1–23.

Greenberg, M. L., and J. P. Castagna, 1992, Shear-wave velocity estimation in porous rocks: Theoretical formulation, preliminary verification and applications: Geophysical Prospecting: 40, 2, 195–209, doi: 10.1111/j.1365-2478.1992.tb00371.x.

Hampson, D. P., B. H. Russell, and B. Bankhead, 2005, Simultaneous inversion of prestack seismic data: 75th Annual International Meetings, SEG, Expanded Abstracts, 1633–1636.

Lumley, D, 4D seismic monitoring of CO2 sequestration, The Leading Edge, Vol. 29, No. 02, 2010

Ma, J, Morozov, I, AVO modeling of pressure- saturation effects in Weyburn CO_2 sequestration, The Leading Edge, Vol. 29, No. 02, 2010

Meadows, M. A., 2013, 4d Rock and Fluid Properties Analysis at the Weyburn Field, Saskatchewan: International Journal of Greenhouse Gas Control, 16, Supplement 1, S134-S45.

Meckel, T. A., R. Treviño, D. L. Carr, A. Nicholson, and K. Wallace, 2013, Offshore CCS in the Northern Gulf of Mexico and the significance of regional structural compartmentalization: Energy Procedia, v. 37, p. 4526–4532.

Mindlin, R. D., 1949, Compliance of elastic bodies in contact: Journal of Applied Mechanics, 16, 259–268.

Nicholson, A. J., 2012, Empirical analysis of fault seal capacity for CO_2 sequestration, Lower Miocene, Texas gulf coast, Master's thesis, The University of Texas at Austin, Austin, Texas, 88 p.

OSMOND, J., 2016, Fault seal and containment failure analysis of a Lower Miocene structure in the San Luis Pass area, offshore Galveston Island, Texas Inner Shelf, Master's thesis, The University of Texas at Austin, 203 p.

Saltzer, R., C. Finn, and O. Burtz, 2005, Predicting V and porosity using cascaded seismic and rock physics inversion: The Leading Edge, **2**4, 732–736, doi: 10.1190/1.1993269.

Sava. D, 2013, Seismic Attribute Sensitivity on CO_2 Saturation: A Rock Physics Study.

Urosevic, M, Pevzer, R, Kepic, A, Wisman, P, Time-lapse seismic monitoring of CO2 injection into a depleted gas reservoir- Naylor Field, Australia, The Leading Edge, 2010, Vol. 20, No. 02

Urosevic, M., R. Pevzner, V. Shulakova, A. Kepic, E. Caspari, and S. Sharma, 2011, Seismic Monitoring of CO_2 Injection into a Depleted Gas Reservoir–Otway Basin Pilot Project, Australia: Energy Procedia, 4, 3550-57

Wallace, K. J., 2013, Use of 3-dimensional dynamic modeling of CO_2 injection for comparison to regional static capacity assessments of Miocene sandstone reservoirs in the Texas State Waters, Gulf of Mexico, Master's thesis, The University of Texas at Austin, Austin, Texas, 139 p.

White, D., 2013, Seismic Characterization and Time-lapse Imaging During Seven Years of CO_2 Flood in the Weyburn Field, Saskatchewan, Canada: International Journal of Greenhouse Gas Control, 16, Supplement 1, S78-S94.

White, D., K. Hirsche, T. Davis, I. Hutcheon, R. Adair, G. Burrowes, S. Graham, R. Bencini, E. Majer, and S. Maxwell, 2000, Theme 2: Prediction, Monitoring and Verification of Co2 Movements: IEA GHG Weyburn CO_2 monitoring and storage project summary report, 2004, 73-148.

Winker, C. D., and M. B. Edwards, 1983, Unstable progradational clastic shelf margins, in D. J. Stanley and G. T. Moore, eds., The shelfbreak: critical interface on continental margins: SEPM Special Publication 33, p. 139-157.

Winker, C. D., and R. T. Buffler, 1988, Paleogeographic evolution of early deep-water Gulf of Mexico and margins, Jurassic to Middle Cretaceous (Comanchean): AAPG Bulletin, v. 72, p. 318–346.

Zoepptiz, K., 1919, Erdbedbenwellen VIIIB, Ueber Reflexion and Durchgang seismischer Wellen durch Unstetigkeistsflaechen: Goettinger Nachrichten, I, 66-84.